Karlsruhe Institute of Technology

# Imaging of subsalt structures with acoustic and elastic Full Waveform Inversion (FWI)

## Abbildung von Strukturen unter Salzkörpern mithilfe der akustischen und elastischen Wellenform-Tomographie

Master Thesis of

## Niklas Thiel

At the Department of Physics
Geophysical Institute

| | |
|---|---|
| Reviewer: | Prof. Dr. Thomas Bohlen |
| Second reviewer: | Prof. Dr. Friedemann Wenzel |
| Advisor: | Dipl.-Ing. Anna Przebindowska |
| Second advisor: | Dr. André Kurzmann |

Duration: 24. October 2012 – 27. September 2013

I declare that I have developed and written the enclosed thesis completely by myself, and have not used sources or means without declaration in the text.

**PLACE, DATE**

. . . . . . . . . . . . . . . . . . . . . . . . . . . . . . . . . . . . . . . .

(**Niklas Thiel**)

# Contents

# 1. Introduction and Motivation

The demand for hydrocarbons is huge and will continue to be huge in the next years. Therefore, energy companies keep looking for new reservoirs but the discovery of new hydrocarbons becomes increasingly challenging (Leveille et al., 2011). In the past, salt basins proved to be successful sites for the search. The most well-known site of salt basins in connection with hydrocarbons is the Gulf of Mexico (GoM).

For classical imaging techniques the reconstruction of structures beneath or near salt bodies is challenging (e.g., Ravaut et al., 2008). The main reason is the geomechanical characteristics of salt bodies. The salt was deposited millions of years ago and other sediments deposited on top. Using openings in the sediments on top of the salt layer the salt moved upwards, driven by the surcharge, and formed canopies. Therefore, the shapes of salt bodies and salt layers are normally very complex. In addition to the shape, the allochthonous salt layers often contain trapped sediments and have a rugose surface (Leveille et al., 2011). The intricate shapes and surfaces of salt bodies result in a complex wave propagation. Regions of poor illumination are often present. Additionally, the energy coming up from subsalt regions is weak due to high reflection coefficients at the sediment-salt interfaces. Therefore, classical imaging techniques have problems picturing the flanks, the bottom of the salt and the subsalt area. Consequences could be geological misinterpretations which are very expensive (Ravaut et al., 2008).

For some subsalt imaging problems solutions have already been developed, such as undershooting for smaller salt bodies by using longer offsets. For salt layers even this technique is not applicable. A promising solution for the problem of subsalt imaging is the application of Full Waveform Inversion (FWI). Unlike conventional techniques the entire waveform is used in the FWI approach. Synthetic data is modelled by using a starting model of the subsurface beneath the acquisition profile. The synthetic data is compared with the field data. In order to match the synthetic data to the field data the starting model is updated iteratively. The FWI can help, depending on the acquisition geometry and recorded waves, to improve the depth image considerably, in particular the subsalt area.

In this work the 2D acoustic (e.g., Tarantola, 1984) as well as the 2D elastic FWI in time domain (e.g., Tarantola, 1986; Mora, 1987) is used. The FWI is applied on synthetic marine data, based on a 2D seismic line from the GoM, delivered by Fugro[1]. The main

---

[1] Fugro Multiclient Services, now part of CGG.

focus is on the reconstruction of subsalt structures such as horizontal layers and steep dipping structures.

The content of this work is outlined in the following paragraphs:

Chapter 2 starts with the theoretical explanation of FWI. The time-domain FWI is based on a local optimisation method. Possible solutions of the non-linear inverse problem are presented in section 2.1. Section 2.2 explains the general process of FWI, including the finite difference (FD) forward modelling, the calculation of the data misfit and the gradient, and other FWI-dependent issues.

For the synthetic FWI the true velocity and density models are required. The composition and construction of both models and the acquisition geometry are explained in chapter 3.

The forward modelling approach is described in chapter 4 and used for a study of seismograms, where main events are assigned to different structures in the model. The second section analyses the differences of acoustic and elastic data.

The most simple and fastest approach for the FWI is the usage of acoustic FWI in combination with synthetic acoustic field data, described in chapter 5. The first section 5.1 describes a resolution study for the model, including the salt body, and for the given acquisition geometry. In section 5.2 a study of different starting models is described. This study answers questions about the required quality of a starting model for a successful FWI. In section 5.3 the so-called Flooding Technique is investigated in detail. This multistage inversion strategy requires no a priori information about the salt body. The original approach of Boonyasiriwat et al. (2010) is compared with the modified Flooding Technique (section 5.3.2) proposed in this work. The influence of the frequency content of the data on the FWI result and frequency filtering are discussed in section 5.4.

As the assumption of acoustic field data is unrealistic the acoustic FWI is applied to elastic data in chapter 6. Especially for large data sets the acoustic FWI is not as expensive as the elastic FWI (Vigh et al., 2009). The FWI experiment in section 6.1 uses a starting model including the salt at the exact location and with the correct shape. In order to compare the acoustic and elastic data the elastic data was converted in pressure data. The comparison revealed an increase of the data differences with offset. Therefore, a limitation of the offset is analysed and described in section 6.2. The results of the modified Flooding Technique using the acoustic FWI with elastic data are discussed in section 6.3.

The results of the acoustic FWI with acoustic and elastic data showed high differences which are summarised and compared in chapter 7.

As the acoustic FWI cannot explain the elastic data completely, the elastic FWI is applied to elastic data in a first test (chapter 8). The elastic FWI results are analysed in relation to the subsalt imaging problem and compared with the results of the acoustic inversion.

The summary of this work and a conclusion can be found in chapter 9.

# 2. Full Waveform Inversion

Most geophysical problems are inverse problems. We would like to reconstruct an underground model from the measured field data. The relation between the observable parameters **d** and the aim of the inversion, the model **m**, is generally given by

$$\mathbf{d}^{obs} = \mathbf{d}^{mod}(\mathbf{m}) \tag{2.1}$$

with the non-linear forward operator $\mathbf{d}^{mod}$ (Tarantola, 2005).

Full Waveform Inversion (FWI) is one of the methods that can be used to solve a non-linear seismic inverse problem. FWI comprises an iterative inversion in order to find the optimal parameter model. The aim of the acoustic FWI is to find the best P-wave velocity and density model. The elastic FWI includes also the S-wave model. The iterative process of FWI is based on two main steps: the forward modelling and the inversion.

For the forward modelling, synthetic data is generated for a starting model (chapter 2.2.1). Some important aspects have to be taken into account during the modelling. These are, for instance, the boundary conditions that aim to prevent edge effects (chapter 2.2.1.1) or the rules for defining the spatial grid spacing and the sampling rate (chapter 2.2.1.2).

The inversion starts with a comparison of the synthetic data and the field data in order to calculate the difference/misfit (chapter 2.2.2). To minimise the data differences and to update the model, a conjugate gradient method is used. After computing the gradient (chapter 2.1) and the step length (chapter 2.2.4), the starting model is updated and the synthetic data is calculated and compared again with the field data. This process is iterated until the synthetic data generated for the final model of the subsurface fits the field data as best as possible. A successful inversion needs an appropriate preconditioning to avoid the problem of local minima. Among others this can be frequency filtering of the synthetic and field data (chapter 2.2.5). Chapter 2.2 describes a detailed scheme of the time-domain FWI.

## 2.1 Inversion of a non-linear problem

Three possible local methods for a solution of a non-linear problem will be introduced in this chapter: the Newton method, the Gauß-Newton method and the conjugate gradient method. The methods' aim is to find the model $\mathbf{m}$ that minimises the data residuals $\delta\mathbf{d} = \mathbf{d}^{mod} - \mathbf{d}^{obs}$.

The most general method is the Newton method: to linearise the inversion problem, the Born approximation is used. The search for the best fitting model $\mathbf{m}$ is performed in the vicinity of the starting model $\mathbf{m}_0$:

$$\mathbf{m} = \mathbf{m}_0 + \delta\mathbf{m} \tag{2.2}$$

with $\delta\mathbf{m}$ as perturbation.

The difference between the modelled and observed data is represented by the objective function, also called misfit function (section 2.2.2). The misfit function $E$ is supposed to be quadratic in the vicinity of the minimum. Therefore, the function can be approximated by a first-order Taylor series around the starting model $\mathbf{m}_0$:

$$E(\mathbf{m}_0 + \delta\mathbf{m}) \approx E(\mathbf{m}_0) + \left(\frac{\partial E(\mathbf{m}_0)}{\partial \mathbf{m}}\right)\delta\mathbf{m} \tag{2.3}$$

At the minimum of the misfit function the first derivative of formula 2.3 must be zero:

$$\frac{\partial E(\mathbf{m}_0 + \delta\mathbf{m})}{\partial \mathbf{m}} = \frac{\partial E(\mathbf{m}_0)}{\partial \mathbf{m}} + \frac{\partial^2 E(\mathbf{m}_0)}{\partial \mathbf{m}^2}\delta\mathbf{m} = 0 \tag{2.4}$$

$$\Leftrightarrow \quad \delta\mathbf{m} = -\left(\frac{\partial^2 E(\mathbf{m}_0)}{\partial \mathbf{m}^2}\right)^{-1}\frac{\partial E(\mathbf{m}_0)}{\partial \mathbf{m}} = -\mathbf{H}^{-1}\nabla_m E(\mathbf{m}_0) \tag{2.5}$$

with the Hessian matrix $\mathbf{H}$. The gradient $\nabla_m E(\mathbf{m}_0)$ can also be written as

$$\nabla_m E(\mathbf{m}_0) = \frac{\partial(\delta\mathbf{d})^T}{\partial \mathbf{m}}\delta\mathbf{d} = \frac{\partial(\mathbf{d}^{mod}(\mathbf{m}) - \mathbf{d}^{obs})^T}{\partial \mathbf{m}}\delta\mathbf{d} = \frac{\partial(\mathbf{d}^{mod}(\mathbf{m}))^T}{\partial \mathbf{m}}\delta\mathbf{d} = \mathbf{F}^T\delta\mathbf{d} \tag{2.6}$$

with the Fréchet matrix $\mathbf{F}$

$$\mathbf{F} = \frac{\partial \mathbf{d}^{mod}(\mathbf{m})}{\partial \mathbf{m}} \tag{2.7}$$

with $\mathbf{d}^{mod}(\mathbf{m})$ as the synthetic data. The Fréchet matrix is also called Jacobi matrix.

Now the model perturbation $\delta\mathbf{m}$ can be expressed as

$$\delta\mathbf{m}^N = -\mathbf{H}^{-1}\mathbf{F}^T\delta\mathbf{d}\,. \tag{2.8}$$

The model update with the Newton method is performed as

$$\mathbf{m}_i = \mathbf{m}_{i-1} - \delta\mathbf{m}_{i-1}^N\,. \tag{2.9}$$

The Hessian matrix $\mathbf{H}$ can be written as

$$\mathbf{H} = \underbrace{\mathbf{F}^T\mathbf{F}}_{\mathbf{H}_a} + \underbrace{\frac{\partial \mathbf{F}^T}{\partial \mathbf{m}}\delta\mathbf{d}}_{\mathbf{H}_e} = \mathbf{H}_a + \mathbf{H}_e\,. \tag{2.10}$$

The computation of the full Hessian matrix $\mathbf{H}$ would require the calculation of the second order derivative of $\mathbf{d}^{mod}$ in $\mathbf{H}_e$. This would lead to high computational costs (Pratt et al., 1998). For the Gauss-Newton method the Hessian matrix $\mathbf{H}$ is approximated by the first term $\mathbf{H}_a$.

If we assume small residuals and a quasi-linear forward equation, the second term $\mathbf{H}_e$ is very small and can be neglected (Pratt et al., 1998). The gradient of the Gauß-Newton method is now the following (similar to equation 2.8):

$$\delta\mathbf{m}^{GN} = -\mathbf{H}_a^{-1}\mathbf{F}^T\delta\mathbf{d} \tag{2.11}$$

The inversion of $\mathbf{H}_a$ assumes that the matrix has a full rank. Usually this is not the case and the matrix must be regularised by a damping factor $\kappa$ (Pratt et al., 1998):

$$\delta\mathbf{m}^{GN} = -(\mathbf{H}_a + \kappa\mathbf{I})^{-1}\mathbf{F}^T\delta\mathbf{d} \tag{2.12}$$

with $\mathbf{I}$ as identity matrix. This method is called Marquardt method.

The third method is the conjugate gradient method. The standard gradient method searches along the direction of the steepest descent for the minimum of the misfit function:

$$\delta\mathbf{m}^{G} = \mathbf{F}^T\delta\mathbf{d} \tag{2.13}$$

The model is updated as follows:

$$\mathbf{m}_i = \mathbf{m}_{i-1} + \mu_{i-1}\,\delta\mathbf{m}^G_{i-1} \tag{2.14}$$

with $\mu$ as step length (see also chapter 2.2.4).

The conjugate gradient method can be applied for a better convergence (Mora, 1987). It searches along the conjugate direction:

$$\delta\mathbf{c}_i = \delta\mathbf{m}^G_i + \gamma_i\,\delta\mathbf{c}_{i-1} \tag{2.15}$$

with the parameter $\gamma_i$ after Polak and Ribiére (Nocedal and Wright, 1999):

$$\gamma_i = \frac{(\delta\mathbf{m}^G_i)^T(\delta\mathbf{m}^G_i - \delta\mathbf{m}^G_{i-1})}{(\delta\mathbf{m}^G_{i-1})^T\delta\mathbf{m}^G_{i-1}} \tag{2.16}$$

The first model update is performed after formula 2.14. Starting from the second iteration the model is updated as follows:

$$\mathbf{m}_i = \mathbf{m}_{i-1} + \mu_{i-1}\,\delta\mathbf{c}_{i-1} \tag{2.17}$$

## 2.2 The process of FWI

The process of pure time-domain FWI is shown in Figure 2.1. The residuals $\delta\mathbf{d}$ are calculated by subtracting the field data $\mathbf{d}^{obs}$ from the synthetic data $\mathbf{d}_i^{mod}(\mathbf{m})$ depending on the current model $\mathbf{m}$, for every iteration $i$ and shot $s$:

$$\delta\mathbf{d}_{i,s} = \mathbf{d}^{mod}_{i,s}(\mathbf{m}) - \mathbf{d}^{obs}_s \tag{2.18}$$

To obtain the best model the data residuals $\delta\mathbf{d}$ must be minimised. In order to do so, the misfit function $E$ of the data need to be expressed by one suitable norm. During the FWI, the norm is minimised. A detailed description of the misfit function can be found in section 2.2.2.

The final gradient is a summation of the gradients for all individual shots:

$$\delta \mathbf{m}_i = \sum_{s=1}^{N_s} \nabla_m E_{i,s} \tag{2.19}$$

The calculation of the gradient is explained in detail in chapter 2.2.2.

For the update of the model, the step length $\mu_i$ is calculated in each iteration to scale the gradient (chapter 2.2.4). The step length is multiplied with the gradient field and subtracted from the previous model:

$$\mathbf{m}_i = \mathbf{m}_{i-1} - \mu_i \, \delta \mathbf{m}_{i-1} \tag{2.20}$$

The new synthetic data is obtained by forward modelling from the updated model. Afterwards the data residuals and the misfit function are calculated again. The iteration follows the steps as described above until a stop criterion is met. As stop criterion the minimisation of the data residuals or a specified maximum iteration number can be used. The result is the model that fits best.

FWI delivers no unique solution, just one model that describes the data as best as possible. There might be other models which describe the data just as well. It is possible to reduce the ambiguity of the inverse problem by adding a priori information. This information can be the sea floor topography, or the top line of the salt body extracted by conventional processing. Also incorporating information such as a velocity trend in the subsurface is useful for the result of the FWI.

### 2.2.1 Finite difference forward modelling

The general wave equation for seismic forward propagation in the time domain is described for the spatial coordinates $\mathbf{x}$ and time $t$ as (Virieux and Operto, 2009):

$$\mathbf{M}(\mathbf{x}) \frac{d^2 \mathbf{d}(\mathbf{x}, t)}{dt^2} = \mathbf{A}(\mathbf{x}) \mathbf{d}(\mathbf{x}, t) + \mathbf{s}(\mathbf{x}, s) \tag{2.21}$$

with $\mathbf{M}$ as mass matrix, $\mathbf{A}$ as stiffness matrix, $\mathbf{s}$ as source term and $\mathbf{d}$ as seismic wavefield. The seismic wavefield represents the pressure in the acoustic case, or the particle velocities in spatial directions in the elastic case. The wave equation is solved by using the Finite-Difference (FD) method.

The Einstein notation is used in the following section for the readers convenience. It implies a summation over a set of indexed terms and omits the sigma sign.

To model the wave propagation, the equation of motion is needed to describe the physical processes in a 3D elastic continuum:

$$\rho \frac{\partial^2 u_i}{\partial t^2} = \frac{\partial \sigma_{ij}}{\partial x_j} \tag{2.22}$$

with $\rho$ as density, $u_i$ the displacement and $\sigma_{ij}$ the stress tensor (Aki and Richards, 1980):

$$\sigma_{ij} = \lambda \Theta \delta_{ij} + 2\mu \epsilon_{ij} \tag{2.23}$$

with $\lambda$ and $\mu$ as the Lamé constants, $\Theta = \epsilon_{kk}$, $\delta_{ij}$ as Kronecker's delta and the strain tensor:

$$\epsilon_{ij} = \frac{1}{2} \left( \frac{\partial u_i}{\partial x_j} + \frac{\partial u_j}{\partial x_i} \right) \tag{2.24}$$

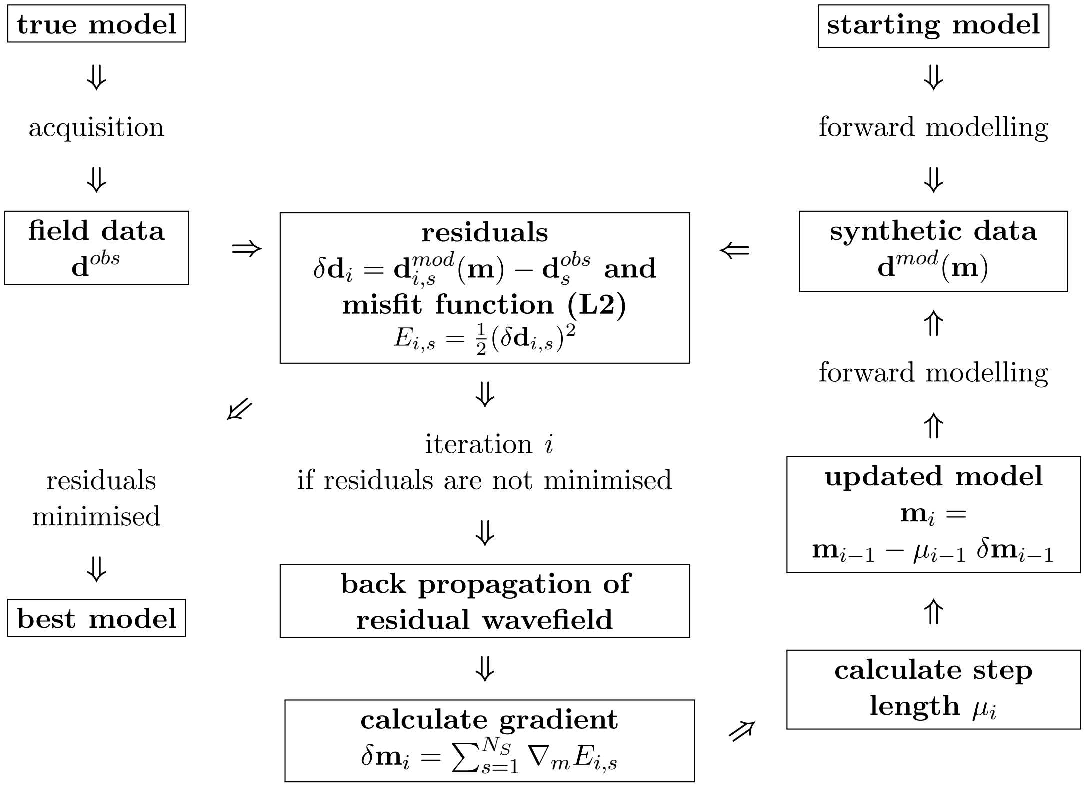

Figure 2.1: Scheme of FWI in the time domain after Tarantola (1984) and Kurzmann (2012).

Hooke's law gives the relation between the stress tensor $\sigma_{ij}$ and the strain tensor $\epsilon_{kl}$ for elastic media:

$$\sigma_{ij} = c_{ijkl}\epsilon_{kl} \tag{2.25}$$

with $c_{ijkl}$ as elastic constants (Lay and Wallace, 1995).

In the acoustic case the 2D wave equation is based on the pressure $p$:

$$\frac{1}{v_P^2(\mathbf{x})\rho(\mathbf{x})}\frac{\partial^2 p(\mathbf{x},t)}{\partial t^2} = \nabla\left(\frac{1}{\rho(\mathbf{x})}\nabla p(\mathbf{x},t)\right) \tag{2.26}$$

#### 2.2.1.1 Boundary conditions

Boundary conditions have to be defined to take the limited size of the model into account. The modelling codes used in this work apply an enhanced form of the absorbing boundary conditions. This so-called Perfectly Matched Layer (PML) is based on the publications Collino and Tsogka (2001), Komatitsch and Martin (2007), and Martin and Komatitsch (2009). The absorbing boundaries condition uses a frame of typically 30 grid points where the values of the stress and particle velocity are damped by an exponential factor. PMLs utilise a coordinate stretch of the wave equation in the frequency domain.

#### 2.2.1.2 Grid dispersion and Courant criterion

To avoid grid dispersion, the minimal wavelength $\lambda_{min}$ has to be at least double the length of the the grid spacing $\Delta h$:

$$\Delta h = \frac{\lambda}{2} \tag{2.27}$$

This formula is called the Nyquist criterion. It is only valid for analytic solutions. To avoid grid dispersion for numerical codes, the spatial grid spacing $\Delta h$ needs to fulfil the following criterion:

$$\Delta h \leq \frac{\lambda_{min}}{n} = \frac{v_{min}}{n f_{max}} \tag{2.28}$$

with $n$ as the number of grid points per wavelength, $v_{min}$ as the minimum velocity in the model and $f$ as the frequency.

In analogy to the spatial discretisation, the temporal discretisation $\Delta t$ must satisfy the sampling criterion as well, known as Courant criterion or Courant-Friedrichs-Lewy criterion (Courant et al., 1928, 1967):

$$\Delta t \leq \frac{\Delta h}{c\sqrt{3}\, v_{p,max}} \tag{2.29}$$

with $c$ as a factor depending on the order of the FD-operator and $v_p$ as the P-wave velocity. In this work a second-order FD scheme is used resulting in $c = 1.0$.

### 2.2.2 Misfit

To assess whether the model is optimal or not an objective evaluation is needed. The evaluation is based on a misfit function and represents a measure of the difference between the modelled and observed data. The misfit function can be defined by the squared residuals $\delta\mathbf{d}$ between the modelled data $\mathbf{d}^{mod}(\mathbf{m})$ and the field data $\mathbf{d}^{obs}$ (least-squares norm, Choi and Alkhalifah, 2012):

$$E^{L2}_{i,s} = \frac{1}{2} \delta\mathbf{d}^{T}_{i,s}\, \delta\mathbf{d}_{i,s} \tag{2.30}$$

To make the objective function more robust against energy differences between the modelled data and field data, the normalised least-squares function can be used (Choi and Alkhalifah, 2012):

$$E^{L2norm}_{i,s} = \frac{1}{2} \delta\hat{\mathbf{d}}^{T}_{i,s}\, \delta\hat{\mathbf{d}}_{i,s} \tag{2.31}$$

with the normalised residuals

$$\delta\hat{\mathbf{d}}_{i,s} = \frac{\mathbf{g}_{i,s}(\mathbf{m})}{\|\mathbf{g}_{i,s}(\mathbf{m})\|} - \frac{\mathbf{d}_s}{\|\mathbf{d}_s\|}\,. \tag{2.32}$$

The normalisation is done for every trace individually. In the following the least-squares function is used in most cases. If a different misfit function is used it is declared.

### 2.2.3 Gradient computation

For the acoustic inversion the gradients are based on the pressure $p$. The gradients for the individual model parameters are given by (Tarantola, 1984; Kurzmann, 2012):

$$\begin{aligned} \delta\mathbf{v}_P &= \frac{\partial\boldsymbol{\kappa}}{\partial\mathbf{v}_P}\delta\hat{\kappa}(\mathbf{x}) + \Delta\mathbf{v}_P \\ \delta\rho(\mathbf{x}) &= \frac{1}{\rho^2(\mathbf{x})}\int dt \sum_s \nabla p(\mathbf{x}_s,\mathbf{x}_r,t)\nabla p'(\mathbf{x}_s,\mathbf{x}_r,t) \end{aligned} \tag{2.33}$$

with $\mathbf{x}_s$ as coordinates of the source and $\mathbf{x}_r$ as coordinates of the receivers, $\rho$ as the density and $\kappa$ as the bulk modulus

$$\kappa = v_P^2 \rho \,. \tag{2.34}$$

For the back propagation the receiver positions are used as source positions and vice versa. With a forward modelling scheme, the residual wavefield is back propagated in time. By cross-correlating (multiplication in time) of the initial wavefield $p$ and the back propagated residual wavefield $p'$ the model update for the P-wave velocity and the density are calculated (equation 2.33). The updates of the individual parameter models are computed by equation 2.20 with $\mathbf{m}_i$ as $v_P$ and $\rho$.

For the gradient computation in the elastic FWI the particle displacement $u$ is used (Köhn, 2011). The gradient expressions for $v_P$, $v_S$ and $\rho$ are given by:

$$\begin{aligned} \delta v_P &= 2\rho v_P \delta\lambda \\ \delta v_S &= -4\rho v_S \delta\lambda + 2\rho v_S \delta\mu \\ \delta\rho_{vel} &= (v_P^2 - 2v_S^2)\delta\lambda + v_S^2 \delta\mu + \delta\rho \end{aligned} \tag{2.35}$$

The gradients of the Lamé parameters can be expressed as sum over all sources $s$ of the integral over time:

$$\begin{aligned} \delta\lambda &= -\sum_s \int dt \left(\frac{\partial u_x}{\partial x} + \frac{\partial u_y}{\partial y}\right)\left(\frac{\partial u_x'}{\partial x} + \frac{\partial u_y'}{\partial y}\right) \\ \delta\mu &= -\sum_s \int dt \left(\frac{\partial u_x}{\partial x} + \frac{\partial u_y}{\partial y}\right)\left(\frac{\partial u_x'}{\partial x} + \frac{\partial u_y'}{\partial y}\right) + 2\left(\frac{\partial u_x}{\partial x}\frac{\partial u_x'}{\partial x} + \frac{\partial u_y}{\partial y}\frac{\partial u_y'}{\partial y}\right) \\ \delta\rho &= \sum_s \int dt \left(\frac{\partial u_x}{\partial t}\frac{\partial u_x'}{\partial t} + \frac{\partial u_y}{\partial t}\frac{\partial u_y'}{\partial t}\right) \end{aligned} \tag{2.36}$$

where $u'$ describes the wavefield obtained by a back propagation of the residual data $\delta\mathbf{u}$. The wavefield $u$ describes the forward propagated wavefield.

### 2.2.4 A selection of an accurate step length $\mu$

An accurate step length parameter $\mu$ is fundamental for a successful inversion (Kurzmann et al., 2008). To find the optimal step length, $\mu$ is calculated for every iteration by a parabolic fitting method (Kurzmann et al., 2009). Therefore, three test models $\mathbf{m}_{test,1}$, $\mathbf{m}_{test,2}$, and $\mathbf{m}_{test,3}$ are calculated with three different test step lengths $\mu_1$, $\mu_2$, and $\mu_3$. The corresponding data misfits are calculated and plotted against the step length. A parabola is fitted through the three points as shown in Figure 2.2. The parabola approximates the true misfit function. The minimum of this parabola represents the optimal step length $\mu_4$. A detailed description can be found in Kurzmann et al. (2009).

### 2.2.5 Preconditioning – frequency filtering

For the inversion a multi-scale approach is used, i.e. the frequency content of the data is gradually increased (Bunks et al., 1995; Sirgue, 2006). In the first stage the modelled and observed data are filtered by a defined lowpass filter. By fitting the synthetic low-frequency data to the low-pass filtered observed data, the risk of cycle skipping is reduced and large

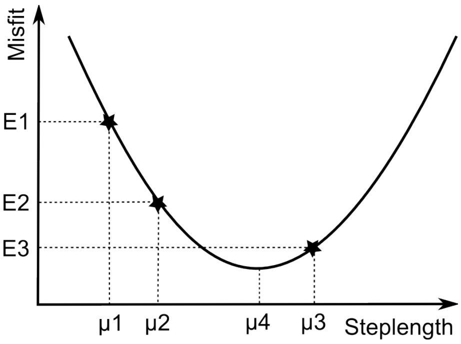

Figure 2.2: Finding the optimal step length by fitting a parabola through three points. The optimal step length $\mu_4$ is the minimum of the parabola.

structures can be included in the model. By increasing the frequency content of the data systematically, more and more details can be reconstructed.

By using optimal frequency bands (Figure 2.3) the number of required iterations per frequency stage can be minimised. To calculate the frequency bands, the following formula is used (Sirgue and Pratt, 2004):

$$f_{n+1} = \frac{f_n}{\alpha_{min}} \tag{2.37}$$

with $f_n$ as the current cutoff frequency, $f_{n+1}$ as next frequency and

$$\alpha = \frac{z}{\sqrt{h^2 + z^2}} \tag{2.38}$$

with $h$ as the maximum half offset and $z$ as the maximum target depth. This method ensures the continuous coverage of vertical wave numbers.

The minimum frequency was set to 3 Hz if not declared otherwise. The maximum frequency is 10 Hz. With a half offset of $h = 4750\,\mathrm{m}$ and a maximum depth of $z = 6000\,\mathrm{m}$ the parameter $\alpha \approx 0.78$ is obtained. Based on formula 2.37 the following cutoff frequencies for the low-pass Butterworth filter were defined:

$$\begin{aligned} f_1 &= 3.0\,\mathrm{Hz} \\ f_2 &= 3.8\,\mathrm{Hz} \\ f_3 &= 4.9\,\mathrm{Hz} \\ f_4 &= 6.2\,\mathrm{Hz} \\ f_5 &= 7.9\,\mathrm{Hz} \\ f_6 &= 10.0\,\mathrm{Hz} \end{aligned}$$

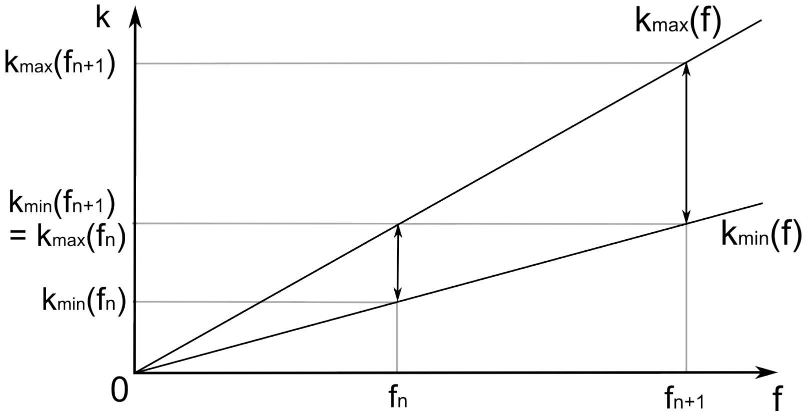

Figure 2.3: Choosing optimal frequencies, after Sirgue and Pratt (2004). The vertical wave number $k$ is plotted against the frequency $f$. The frequencies are chosen to allow a continuous coverage of vertical wave numbers with a minimum number of frequency bands.

### 2.2.6 Relative model error

In order to estimate the quality of a FWI result the relative model error RME is used in this work. The RME is calculated by using the FWI model result *inv* and the true model *true*:

$$\mathrm{RME} = \frac{1}{I \cdot J} \sum_{ij} \frac{|inv_{ij} - true_{ij}|}{|true_{ij}|} \tag{2.39}$$

$I$ and $J$ are the dimensions of the model matrices. The absorbing boundaries are excluded in the RME calculation due to the marginal model update.

An increase of the RME can occur during the FWI despite of an apparent improvement of the model. Artefacts are the main reason for this kind of increase. Therefore, the RME value has to be considered carefully.

### 2.2.7 Software

All modelling and inversion tests presented in this work were performed with a 2D acoustic FWI (Kurzmann, 2012) and the elastic FWI DENISE (subwavelength DEtail resolving Nonlinear Iterative SEismic inversion), developed by Köhn (2011).

The parallelisation of both codes is based on domain decomposition where the model is decomposed in subgrids (e.g., Bohlen, 2002). The subgrids must be larger than the absorbing boundary of 30 grid points (chapter 2.2.1.1). Consequently, the model with the size of 850x532 grid points can be decomposed in a maximum of $25 \cdot 14 = 350$ subgrids. The acoustic code has a shot parallelisation implemented. The distribution of shots on different computers provides a reduction of network traffic and consequently a speedup of the inversion algorithm (Kurzmann et al., 2009).

A Ricker wavelet is used as pulse of the explosive source (Ricker, 1953). All settings of the parameters for the modelling and the inverted models are presented in chapter 3. Furthermore, individual parameters that were set and tested can be found in the description of the inversion results.

# 3. Model description and acquisition geometry

## 3.1 True models

The modelling of synthetic acoustic and elastic data needs true models. For the acoustic modelling a P-wave velocity model and a density model are required. The elastic modelling needs an S-wave model in addition. The composition of the models is described in the next sections.

### 3.1.1 P-wave velocity model

For the synthetic FWI tests a subset of the migration velocity model (Figure 3.1) was selected in consultation with Fugro. This subset includes a salt body in varying depth and steep slopes. Undershooting cannot be performed as the salt body extends over the entire horizontal dimension. In addition the top of the salt body is located in a shallow part between two to three kilometres. This allows me to limit the size of the model which is important for the reduction of computational time and at the same time include a subsalt area as large as possible. The selected part (Figure 3.2a) has the following dimensions:

- model in x-direction: 10625 m
- model in y-direction: 6250 m

In order to create realistic background structures for the true model, a modified part of the Sigsbee2A model was used (Paffenholz, 2001). The Sigsbee2A model was chosen as true background model due to the fact that it already contains fine sedimentary layers and mimics the geology of the Gulf of Mexico. The P-wave velocity in the background model ranges from 1476 $\frac{\mathrm{m}}{\mathrm{s}}$ to 3300 $\frac{\mathrm{m}}{\mathrm{s}}$. The lowest velocity appears in a horizontal layer in a depth of about 500 m. The salt body from the selected part of the migration velocity model was inserted in the background Sigsbee2A model (Figure 3.3a). An air layer was inserted at the top of the model with a thickness of 400 m. The thickness results from the absorbing frame (chapter 2.2.1.1). The zero position of the y-axis (vertical axis) is the air-water interface.

In the subsalt area two steep faults were inserted. They are used as important features for resolution studies. Apart from these two structures, the subsalt area contains nearly horizontal sediments. Seven circular velocity perturbations of 75 m diameter are included in the model. They are located in a depth of about 2660 m and 3540 m and also used for resolution studies.

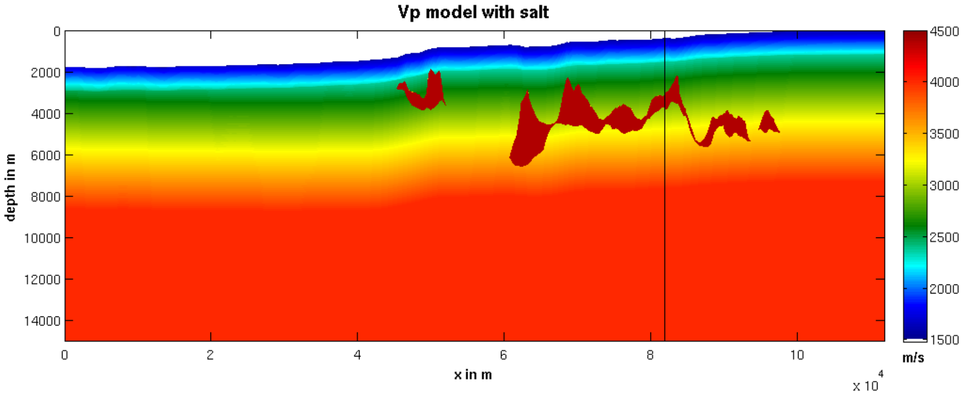

Figure 3.1: Original $v_P$ migration model of the field data from the GoM over the full profile. The vertical black line marks the same location as in Figure 3.2a.

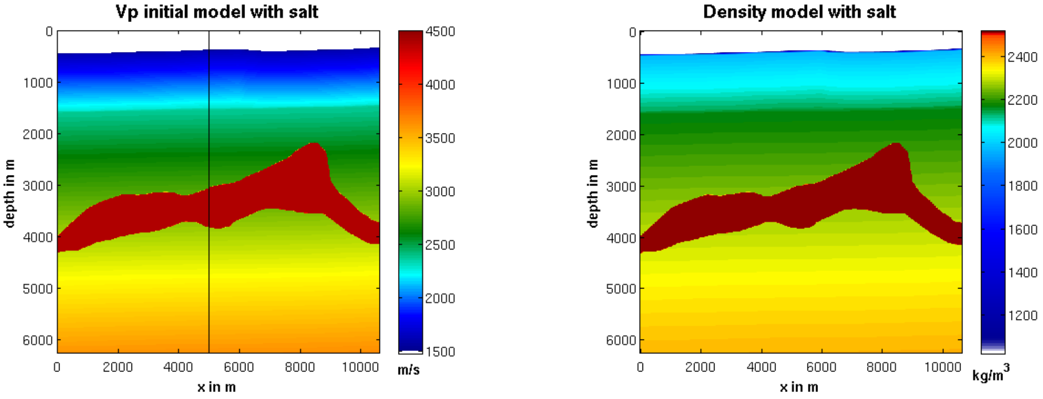

(a) Modified velocity model with the salt body included. The vertical black line marks the same location as in Figure 3.1.

(b) Density model with salt body.

Figure 3.2: Chosen subset of the migration model.

### 3.1.2 Density model

The density $\rho$ in the salt and in the sediment was calculated from the P-wave velocity $v_P$ by using the Gardner relation (Gardner et al., 1974):

$$\rho = 230 \cdot (v_P \cdot k)^{0.25} \tag{3.1}$$

where $k = 0.3048$ is the factor to convert metres in feet. The water density is set to $1020\,\frac{\mathrm{kg}}{\mathrm{m}^3}$ (e.g., Cox et al., 1962) and is assumed to be known during the FWI. The density model can be seen in Figure 3.3b.

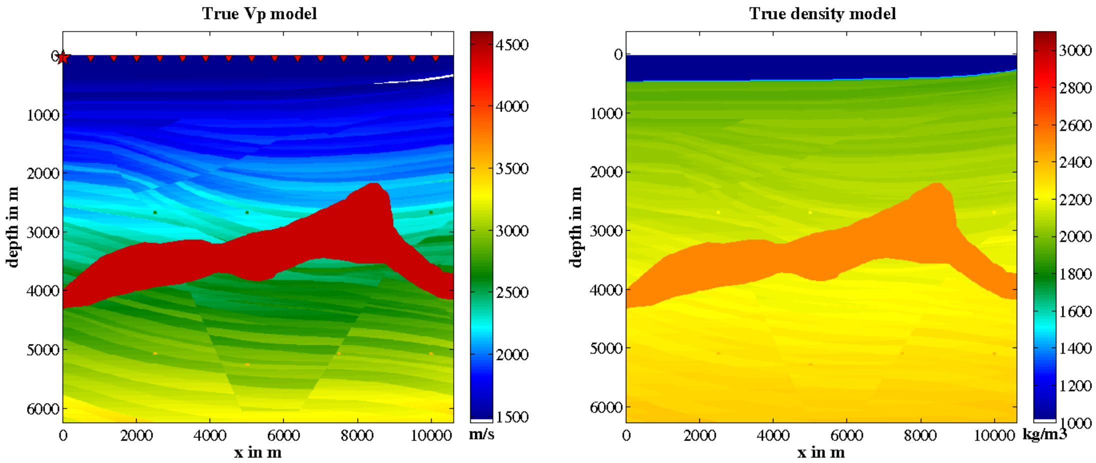

(a) True $v_P$ model.

(b) True density model.

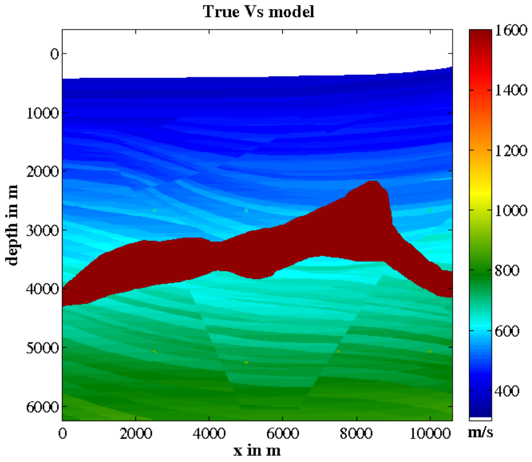

(c) True $v_S$ model. The salt body velocity is 2600 $\frac{\mathrm{m}}{\mathrm{s}}$.

Figure 3.3: Modified part of the Sigsbee2A model including the salt body.

### 3.1.3 S-wave velocity model

The S-wave model was computed from the P-wave velocity model. For salt the Poisson's ratio $\sigma$ varies between 0.2 and 0.3 (Liang et al., 2007). By applying the formula for the $v_P$ to $v_S$ ratio (Reynolds, 1997)

$$\frac{v_P}{v_S} = \left(\frac{1-\sigma}{0.5-\sigma}\right)^{0.5} \tag{3.2}$$

a $\frac{v_P}{v_S}$ ratio of $\sqrt{3}$ is used to compute the shear wave velocity for the salt body.

For sediments a $\frac{v_P}{v_S}$ ratio of 4 was used (Reynolds, 1997). The S-wave velocity model is displayed in Figure 3.3c.

## 3.2 Preparation for modelling

For the modelling and FWI the model was resized to a grid with a grid space of 12.5 m (two times the original spacing). This spacing is small enough for an accurate distribution of receivers and sources and an FD-modelling without numerical dispersion for frequencies below 10 Hz (chapter 2.2.1.2). However, the spacing is large in terms of computational costs/time. To fulfil the Courant criterion (chapter 2.2.1.2) the sampling interval was set to $dt=1.5 \cdot 10^{-3}$ s. The recording time was set to 6 s to observe the waves coming up from the subsalt region. Pressure sources and pressure receivers were used because of the acquisition in a marine environment. The following listing gives an overview of the chosen parameters:

- grid space: 12.5 m
- number of grid points in x-direction (horizontal direction): 850
- number of grid points in y-direction (depth direction): 532
- $dt=1.5 \cdot 10^{-3}$ s
- recording time: 6 s (accordingly 4000 time samples in total)

## 3.3 Acquisition geometry

The acquisition geometry for the FD-modelling is based on the real acquisition geometry of the selected field shot gathers. This is necessary to make the synthetic data comparable to the field data for a future FWI of the field data. The vessel tows the streamer from the right side of the model to the left side. To reduce the computational time, the data was decimated in the shot domain. Every 5th shot was taken, which results in a shot spacing of 187.5 m. In the FD code, sources and receivers are located exactly at a grid point in y-direction and between two grid points in x-direction. Due to the moving geometry and the limited profile, the number of active receivers varies between 16 and 751 (Figure 3.4). The longest offset of 9.5 km is defined for the last shot 50.

In x-direction the sources and receivers are located as listed in table 3.1. In y-direction they are located in a depth of one grid point below the water level. Including the air layer the receivers and sources are located in a depth of 412.5 m below the top edge of the model.

Table 3.1: Location and spacing in x-direction of the sources and receivers in the model.

| description | in grid points | in metres |
|---|---|---|
| last shot (50) location | 48/49 | 606.25 |
| first shot (1) location | 783/784 | 9793.75 |
| first receiver location (shot 1) | 793/794 | 9918.75 |
| first receiver location (shot 50) | 58/59 | 731.25 |
| last receiver location | 808/809 | 10106.25 |
| shot spacing | 14 | 175 |
| receiver spacing | 1 | 12.5 |
| near offset | 10 | 112.5 |
| far offset | up to 760 | up to 9500 |

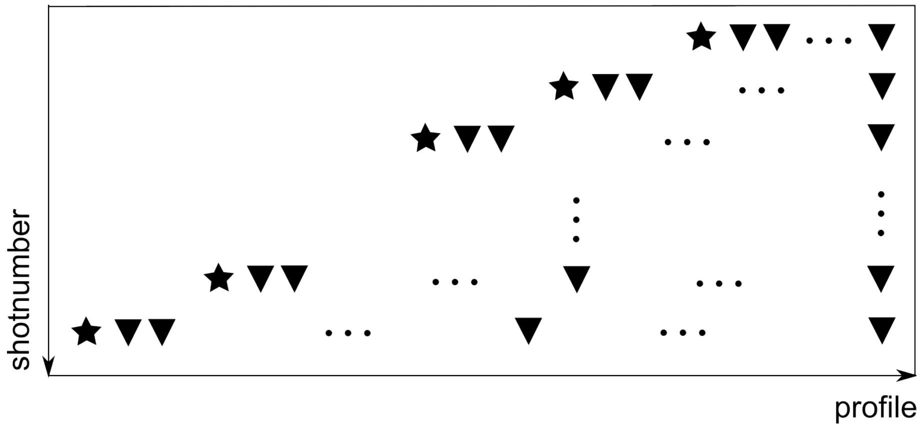

Figure 3.4: Sketch of the acquisition geometry. The stars represent the sources, the triangles the receivers.

# 4. Forward modelling

The aim of the modelling is to produce synthetic data for a given velocity and density model. In this chapter, the 'observed' synthetic data are generated for a true model for FWI studies. The forward modelling was performed as explained in chapter 2.2.1. In the first part of this chapter (section 4.1), I assign the main events in the seismograms to structures in the model. In the second study (section 4.2), I generate acoustic and elastic data for a true model. The elastic data differs from the elastic data as supposed. I analyse the quantity of the differences between the acoustic and elastic data and their potential impact on the acoustic FWI of elastic data in chapter 6.

The used velocity model in this chapter is shown in Figure 4.3a. It includes a velocity gradient with a step as background (cf. Figure 4.3b) and in addition the salt body, a subsalt structure as low velocity layer, and a subsalt reflector.

## 4.1 Seismic data analysis

For a better understanding of the synthetic seismograms, and subsequently the field data, the main events in the seismograms were assigned to structures in the model. Figure 4.2 shows the labelled main events of selected structures of the velocity models displayed in Figure 4.1. The seismograms were calculated by an acoustic forward modelling.

The first seismogram (Figure 4.2a) was modelled by using model 1 in Figure 4.1a as true model. As the subsurface of model 1 only consists of the water layer, the sea bottom with topography and a constant sedimentary half space ($v_P = 1800\,\frac{\mathrm{m}}{\mathrm{s}}$), the resulting seismogram contains the direct wave and the reflection from the sea bottom only.

The second seismogram (Figure 4.2b) shows the result of the subtraction of the seismograms of model 2 (Figure 4.1b) and 1 (Figure 4.1a). In model 2, a depth-dependent velocity gradient replaces the constant sedimentary half-space. The reflection from a step in the gradient at approximately 2 km (see also Figure 4.3b) is visible, also the refracted wave of the sea bottom and the diving wave as result of the depth depending velocity gradient.

The third seismogram in Figure 4.2c is the result of subtracting the seismograms of model 3 (Figure 4.1c) and 2 (Figure 4.1b). Model 3 is identical to model 2 but the salt body is included. The top and bottom salt reflections can be assigned as well as the refracted wave of the top salt.

The fourth seismogram (Figure 4.2d) displays the reflections from the subsalt structure, where the seismogram of model 5 (Figure 4.1e) was subtracted from the seismogram of model 6 (Figure 4.1f). Model 5 contains the velocity gradient without the salt body and a subsalt reflector in a depth of about 5700 m with weak topography and a P-wave velocity of 3800 $\frac{\mathrm{m}}{\mathrm{s}}$. In comparison to model 5, model 6 has a low velocity layer included in a depth of about 5100 m with a P-wave velocity of 2000 $\frac{\mathrm{m}}{\mathrm{s}}$ in addition.

The fifth seismogram (Figure 4.2e) shows information from the subsalt reflector computed by subtracting the seismograms generated for model 6 and 4. The sixth seismogram (Figure 4.4) was modelled for the entire model 7 shown in Figure 4.3a. All main events are labelled. This seismogram displays one of the problems of conventional processing methods: the events of both subsalt structures have very low energy and overlap each other. Even with amplified amplitudes it is impossible to distinguish between these two events visually.

In this section the main events in the seismograms were assigned to structures in the model. This test also demonstrates one of the problems of subsalt imaging when conventional processing methods are applied: the low amplitude events coming from the subsalt area and their overlapping.

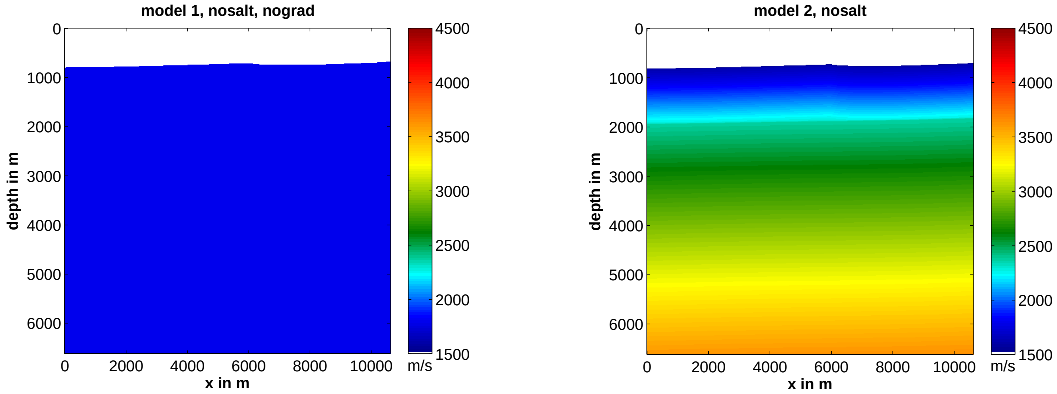

(a) Model 1: homogeneous velocity (1800 $\frac{\mathrm{m}}{\mathrm{s}}$) without structures.

(b) Model 2: velocity gradient (about 1700 – 3600 $\frac{\mathrm{m}}{\mathrm{s}}$) without structures.

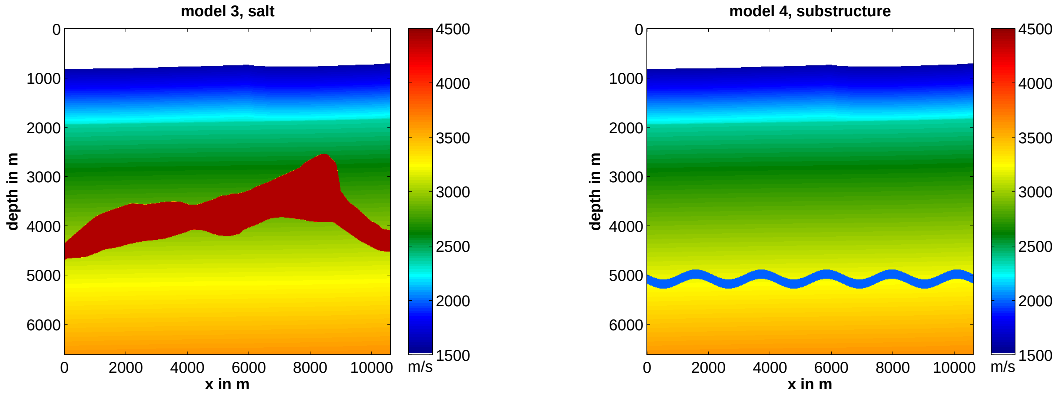

(c) Model 3: velocity gradient with salt body (4400 $\frac{\mathrm{m}}{\mathrm{s}}$).

(d) Model 4: velocity gradient with low velocity layer (2000 $\frac{\mathrm{m}}{\mathrm{s}}$) in a depth of about 5 km.

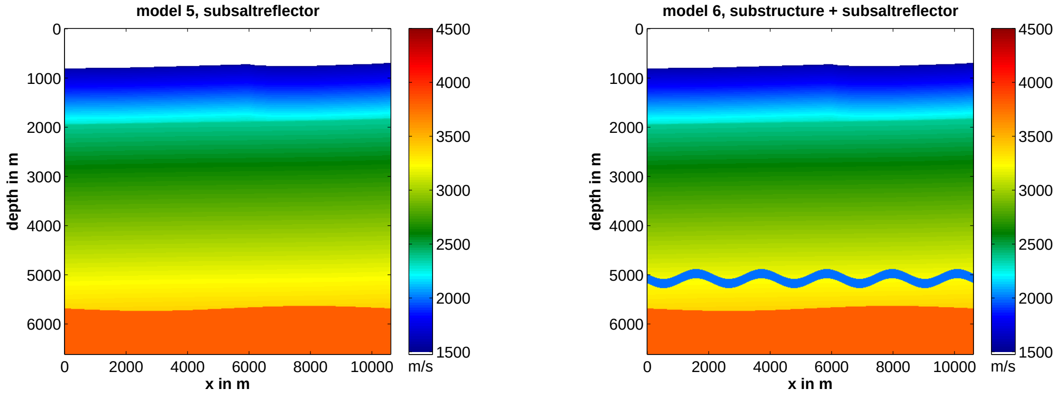

(e) Model 5: velocity gradient with reflector (3800 $\frac{\mathrm{m}}{\mathrm{s}}$) at a depth of about 5.7 km.

(f) Model 6: velocity gradient with low velocity layer (cf. Figure 4.1d) and reflector (cf. Figure 4.1e).

Figure 4.1: The models used for the forward modelling (Figure 4.2).

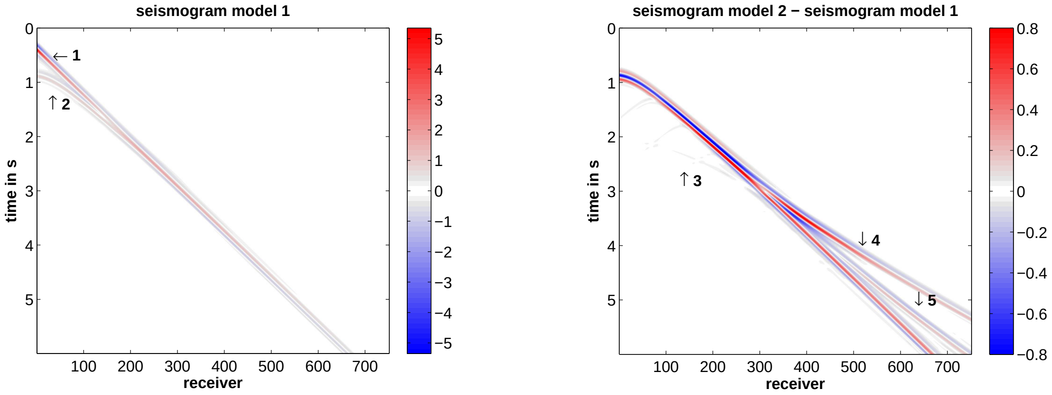

(a) Seismogram of model 1 (main events: 1: direct wave; 2: sea bottom reflection).

(b) Seismogram of model 2 minus seismogram of model 1 (main events: 3: reflection from step in velocity gradient; 4: refracted wave from sea bottom; 5: diving wave).

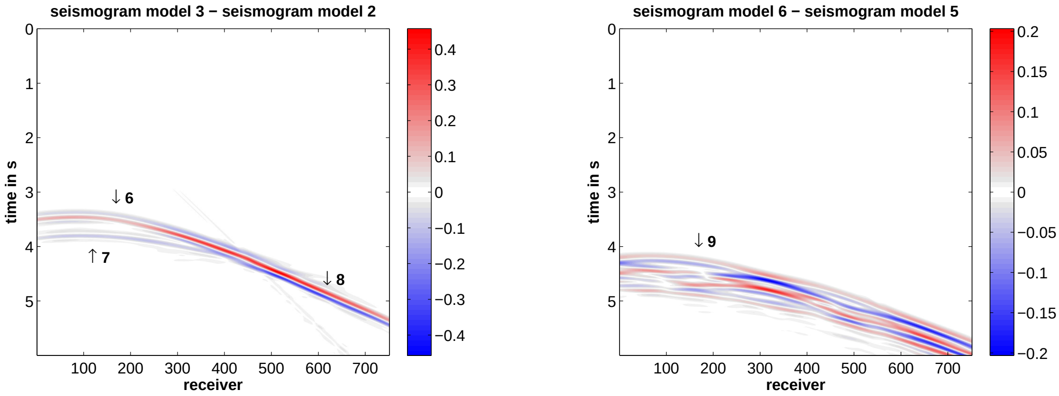

(c) Seismogram of model 3 minus seismogram of model 2 (main events: 6: top salt reflection; 7: bottom salt reflection; 8: refracted waves in the salt body).

(d) Seismogram of model 6 minus seismogram of model 5 (main events: 9: subsalt structure reflection).

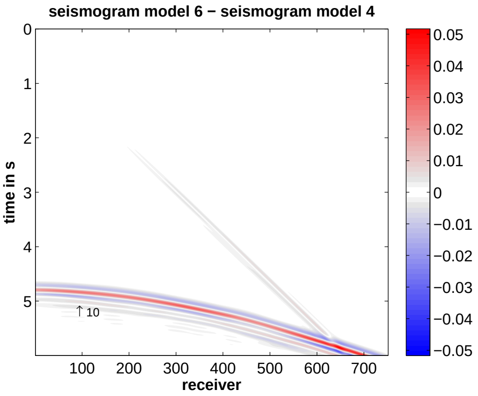

(e) Seismogram of model 6 minus seismogram of model 4 (main events: 10: reflection from the subsalt reflector).

Figure 4.2: Seismograms produced by forward modelling using the models displayed in Figure 4.1. The main events are assigned to structures in the models.

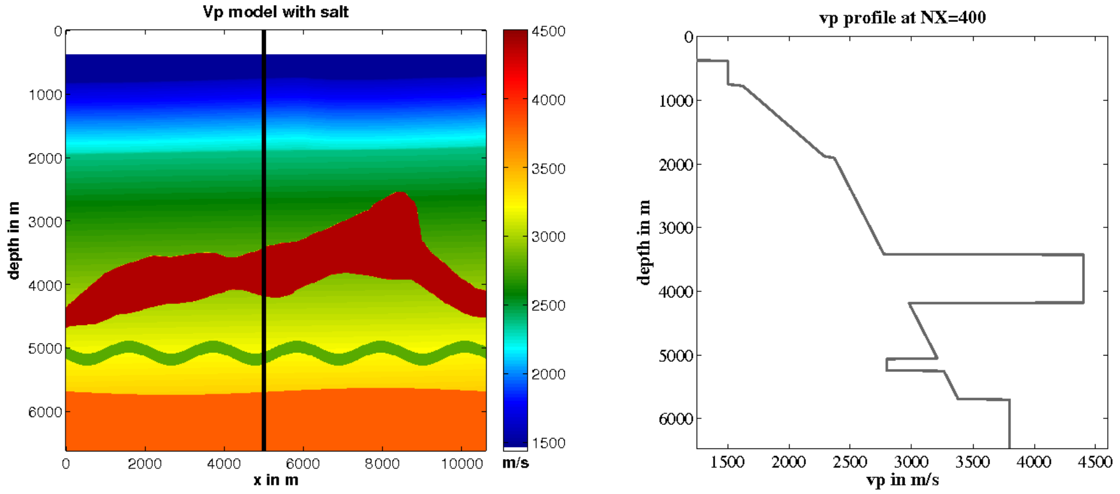

(a) Model 7: all structures described in Figure 4.1 combined.

(b) Velocity profile, located at the black line in Figure 4.3a (x=5000 m).

Figure 4.3: Entire P-wave velocity model including all subsalt structures used for forward modelling.

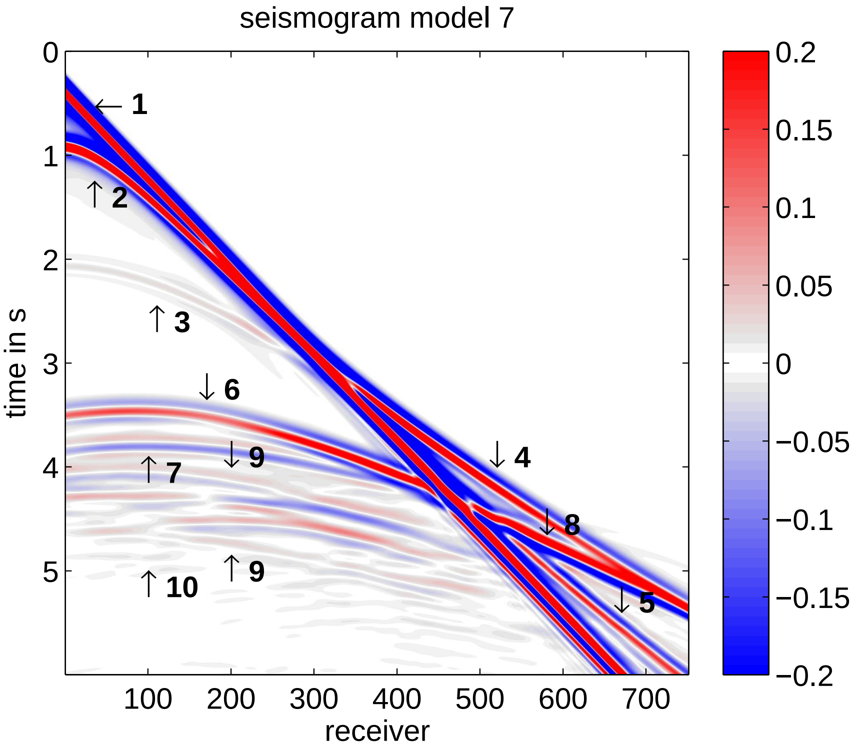

Figure 4.4: Seismogram of model 7 (Figure 4.3a) showing the following main events: 1: direct wave; 2: sea bottom reflection; 3: reflection from step in velocity gradient; 4: refracted wave from sea bottom; 5: diving wave; 6: top salt reflection; 7: bottom salt reflection; 8: refracted wave in the salt body; 9: subsalt structure reflection; 10: reflection from the subsalt reflector.

## 4.2 Elastic vs. acoustic FWI

In reality the waves are travelling through a 3D viscoelastic anisotropic medium. The acoustic code just inverts for acoustic isotropic data. To get a feeling of the differences in the data and the errors in the FWI results, the acoustic and elastic modelled data were compared. The elastic and acoustic modelling was performed with DENISE and both resulting data sets were written out as pressure wavefields. In Figure 4.5 traces for different offsets of acoustic and elastic forward modelled data are displayed. For the modelling the 1D gradient model with the included salt body (model 3 in Figure 4.1c) was used. The seismograms in Figure 4.5 are normalised and the pictures show a selected time period of the events. The entire seismogram for the elastic case is displayed in Figure 4.5f.

The waveforms in Figure 4.5a (trace 5) match almost perfectly for the direct wave and the reflection of the seabed. All differences are within the error of the sampling interval. The same applies for the reflection of the step in the gradient and the reflection of the top and bottom of the salt, visible at trace 100 in Figure 4.5b. The waveforms after the bottom salt reflections differ slightly even for near offsets (trace 5 and 100) (not visible in Figure 4.5a due to the low amplitude). My investigations show that the interfering wavefields of the P- and S-waves are the most likely reason for this. This explanation is supported by the fact that the differences get stronger in the mid-offset range (Figure 4.5c) and decrease again in the far offset (Figure 4.5d and 4.5e). The effect can also be seen by plotting the relative model error for all offsets (Figure 4.7a).

The significant differences between elastic and acoustic wavefields in the mid-offset range can be explained with Figure 4.6a. The graph displays the energy ratio of P-waves as a function of the incidence on an interface. They are calculated with the Zoeppritz equations (CREWES Zoeppritz Explorer Applet, 2013) by using the model displayed in Figure 4.6b. The interfaces used for the calculation is the sediment-salt interface in the Sigsbee2A model in Figure 3.3. The critical incident angle is identified in this figure at about 30°. For incidence angles higher than the critical angle and smaller than 60°, the reflected P-wave (red) has a smaller magnitude than the reflected S-wave (green) (cf., Lin, 2003). That explains why the differences are larger for the mid-offset ranges than for near- and far-offset ranges.

For the more complex model in Figure 3.3 one trace is displayed for different offsets in Figure 4.8 for the acoustic and elastic modelling with DENISE. Due to the more complex wavefield, the effect of the poor matching in the mid-offset is less visible. The fit of both modelling results gets worse with greater offsets. In Figure 4.8a both time series match almost perfectly. For an offset of 2.1 km (Figure 4.8b) the phases agree but the amplitudes differ increasingly with the time. In Figure 4.8c differences in the phase and amplitude are visible from 4.9 s on.

In summary it can be said that the differences in the data of an acoustic and elastic forward modelling are considerable, in spite of a marine acquisition geometry. The differences in the data are a result of converted waves at sediment or salt interfaces. Furthermore, the differences vary with the offset.

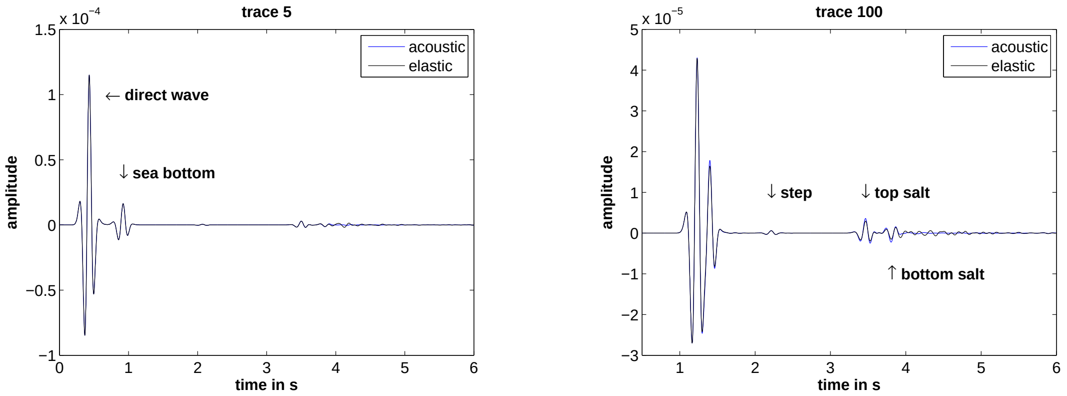

(a) Trace 5, offset: 162.5 m.

(b) Trace 100, offset: 1350 m.

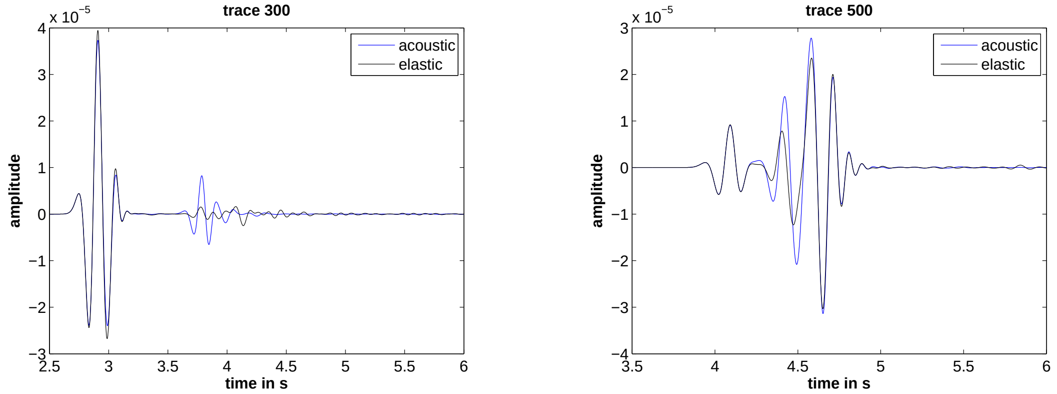

(c) Trace 300, offset: 1850 m.

(d) Trace 500, offset: 6363 m.

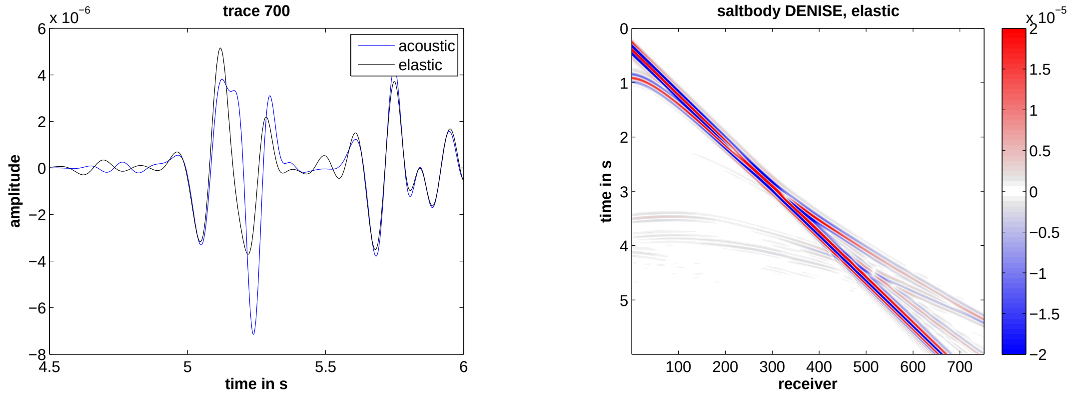

(e) Trace 700, offset: 8863 m.

(f) Full elastic seismogram.

Figure 4.5: Comparison of acoustic and elastic modelled data with DENISE for different offsets. The offset ranges from 162.5 m (trace 5) to 8863 m (trace 700). Model 3 (Figure 4.1c) was used for both modelling tests.

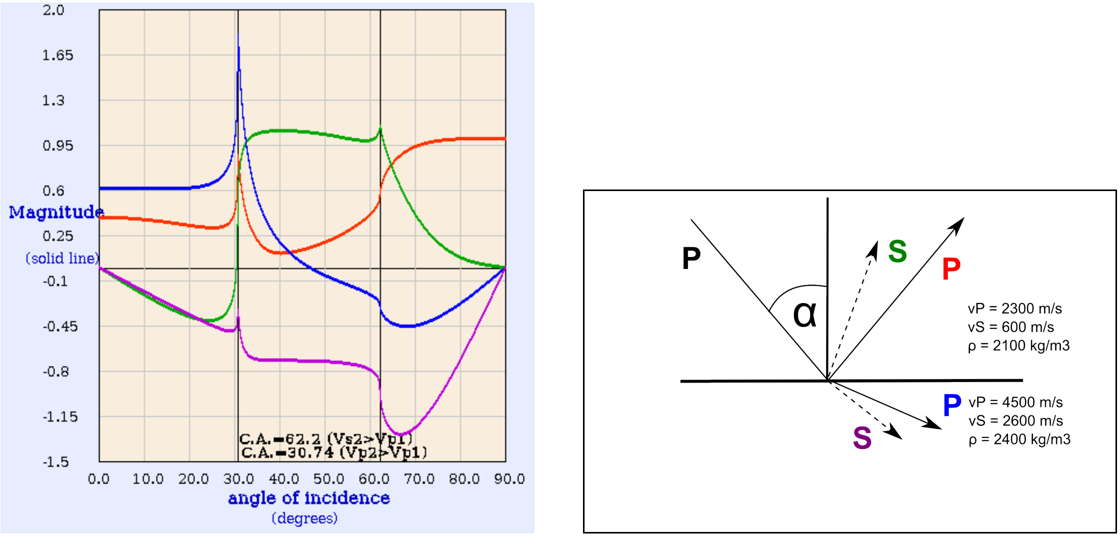

(a) Magnitude of P-waves as a function of the incidence angle on a surface as displayed in Figure 4.6b, calculated with the CREWES Zoeppritz Explorer Applet (2013).

(b) Incident P-wave (incident angle $\alpha$) on an interface and the resulting reflected and transmitted P- and S-waves.

Figure 4.6: Influence of the incident angle of the P-wave (on a sediment-salt interface) on the magnitude of the converted S-waves. Colours: red: reflected P-wave, green: reflected S-wave, blue: transmitted P-wave, and purple: transmitted S-wave.

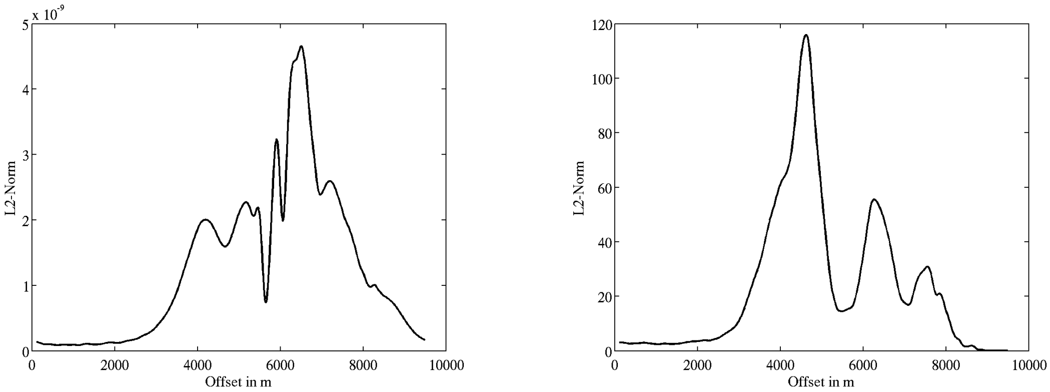

(a) Data calculated with model 3 (Figure 4.1c).

(b) Data calculated with model in Figure 3.3.

Figure 4.7: Least-squares misfit (L2-Norm, section 2.2.2) of the elastic and acoustic data plotted as a function of the offset.

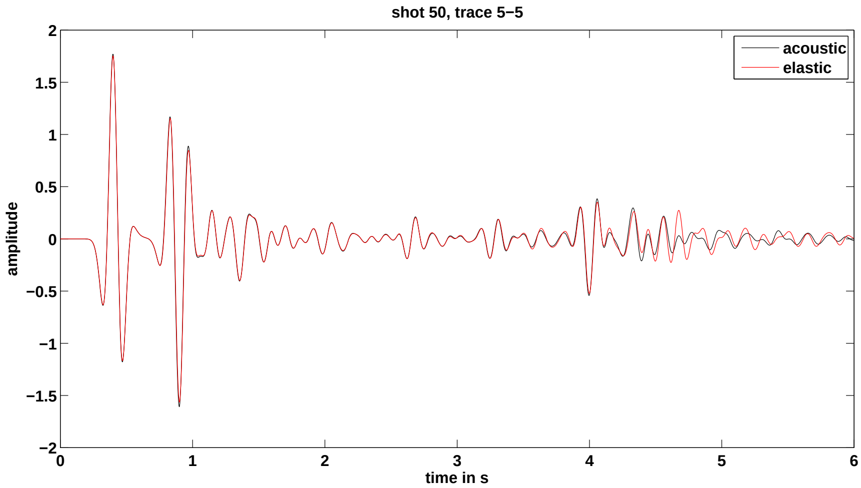

(a) Shot 50, trace 5, offset: 162.5 m.

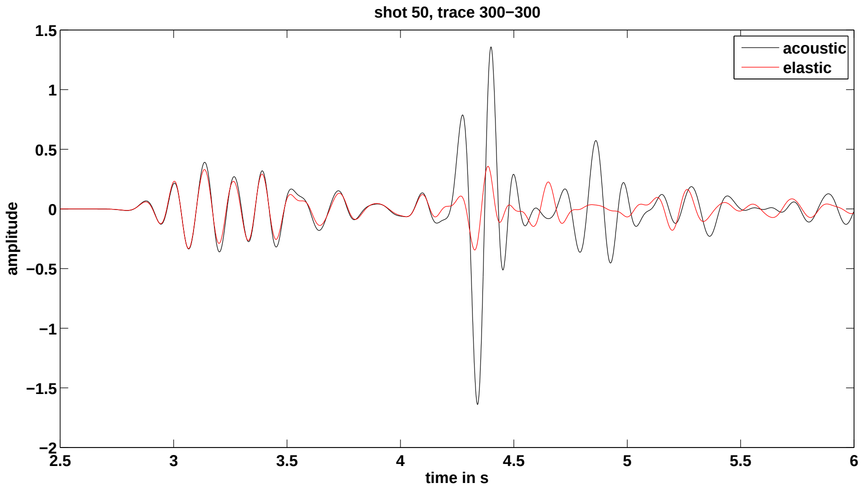

(b) Shot 50, trace 300, offset: 3850 m.

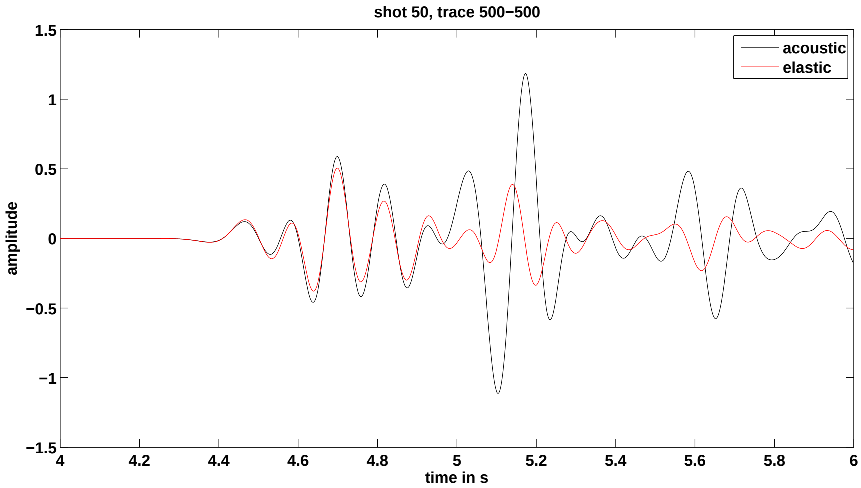

(c) Shot 50, trace 500, offset: 6250 m.

Figure 4.8: Comparison of acoustic and elastic modelled data for different offsets. The modelling was performed with DENISE using the true model displayed in Figure 3.3.

# 5. Acoustic FWI with acoustic data

In the marine environment only acoustic waves are recorded. Therefore, the first study deals with the acoustic FWI only. Shear waves and converted waves are neglected. The first section 5.1 contains a resolution study. This gives an impression of how the resolution varies in different parts of the model due to the model composition and the acquisition geometry. The second section 5.2 analyses the influence of the salt body in the starting model on the FWI result.

Instead of using an optimal starting model another approach can be used, called Flooding Technique. With this method the salt body is reconstructed in several stages in the FWI process (section 5.3).

The least-squares misfit norm (section 2.2.2) was used in the FWIs and the parameters declared in section 3.2. In this chapter frequencies from 1 to 10 Hz were used. The results are comparable to the FWI results with a frequency content of 3 to 10 Hz, as explained in section 5.4.

## 5.1 Checkerboard test

The checkerboard test analyses the resolution of the FWI in a model for a given acquisition geometry and a maximum frequency of the data. The true model is perturbed with a checkerboard-like pattern to vary the velocity of the model in a given range for every rectangle. The starting model does not contain any pattern and the aim of the FWI is to reconstruct the checkerboard.

With a maximum frequency in the data of 10 Hz and a P-wave velocity of 2000-3000 $\frac{\text{m}}{\text{s}}$ the wavelength is 200-300 m. The theoretical resolution of FWI is about half a wavelength. Therefore, the expected resolution is 100-150 m. The checkerboard test was run with the following parameter:

- Edge length: 300 m (equates to double the expected resolution)
- Velocity variation: ±5%

Figure 5.1c shows the true checkerboard velocity model. The starting model contains the salt body and a linear velocity background model (Figure 5.1b).

The final velocity model reconstructed by the FWI is shown in Figure 5.1a and a velocity profile of the result is shown in Figure 5.1d. In the upper part the checkerboard pattern is very well resolved. At the boundaries the PML (section 2.2.1.1) prevents any update in the model resulting in an unmodified area. The middle part of the salt body is also well resolved with smoothed edges. The smoothing is a result of higher velocities which implies a greater wave length. This effect reduces the resolution.

In the subsalt part and at the edges of the salt body the wave paths are clearly visible in the reconstructed pattern. Due to the lack of high frequencies, the higher velocities and the acquisition geometry, the resolution is limited in deeper parts of the model.

The data has a frequency range of 1 to 10 Hz. From chapter 6 on, the frequency band is reduced to more realistic 3 to 10 Hz. This does not affect the checkerboard tests, as low frequencies are not essential for FWI in this work (cf. chapter 5.4). All large-scale objects are included in the starting model. Therefore, the checkerboard test was only performed for a small edge length and not for greater edge length. For a larger pattern the result can be different (Lévêque et al., 1993).

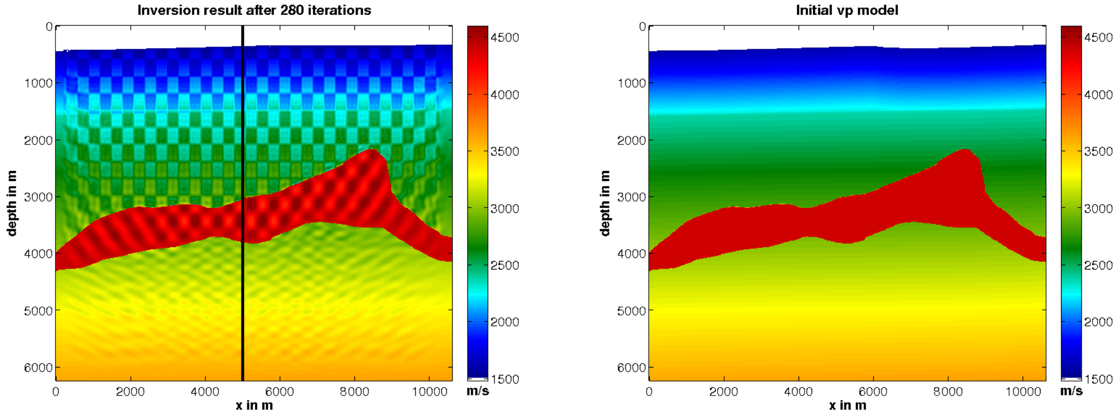

(a) Inverted P-wave velocity model after 280 iterations.

(b) Starting P-wave velocity model.

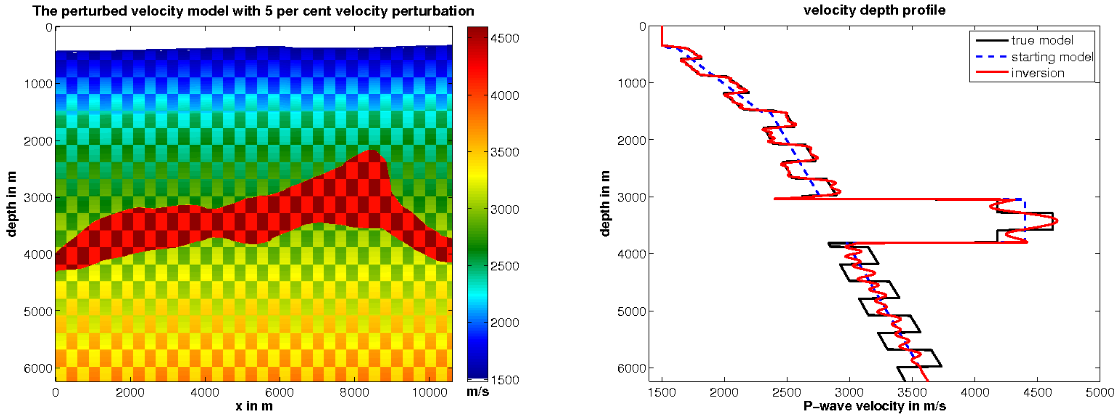

(c) True P-wave velocity model with checkerboard-like perturbation.

(d) Velocity profile located at the black line in Figure 5.1a.

Figure 5.1: Checkerboard test with an edge length of 300 m and a velocity variation of ±5%.

## 5.2 Starting model tests

The choice of a starting model is crucial for the FWI result. The initial synthetic data generated from the starting model must match the waveforms of the observed data within half a cycle (Chauris et al., 2008). Otherwise the FWI fits the wrong cycles of the modelled and real data, leading to an incorrect model update. This effect is called cycle-skipping effect (see also section 5.2.4).

In the next sections the required quality of the starting model is investigated. The main aspects are location, shape and velocity of the salt body (sections 5.2.1 - 5.2.3). I will vary these factors and analyse possible solutions (section 5.2.5).

As background for the starting model a 1D depth-dependent linear gradient is used. In comparison to a starting model obtained by blurring the true model, the 1D linear gradient does not contain any information about structures in the true model.

The water layer is not updated in all FWI experiments as the depth, velocity, and density of the water are well-known. A further advantage is that a gradient preconditioning with respect to the source and receiver artefacts is not necessary.

### 5.2.1 Correct location of the salt body

In the following test the salt body is included in the starting model (Figure 5.2b). The FWI result in Figure 5.2a is very well resolved. The velocity profile in Figure 5.2d shows an almost perfect conformity of the FWI result with the true model in the part above the salt body. The subsalt part is also well resolved. All layers are detected and the velocity is reconstructed sufficiently.

This example shows the potential of FWI with a good starting model, particularly with regards to the subsalt area.

### 5.2.2 No salt body

If the starting model does not contain any information about the salt body (Figure 5.3b) the FWI computes the result shown in Figure 5.3a. The recovered velocity model contains various minor and major artefacts, especially around the salt body. Apart from the artefacts, the layers above the salt are reconstructed but they are shifted upwards (see the velocity profile in Figure 5.3d). The top of salt is detected, but also mislocated by approximately 75 m above the actual top edge of the true salt body. Below the salt body no structures in the sediment are reconstructed.

The FWI result of this section displays the necessity to include additional information about the shape, velocity and location of the salt body. In the next sections the influence of these parameters on the result are tested.

### 5.2.3 Incorrect location of the salt body

If the shape and velocity of the salt body is given, how accurate does the position have to be? To answer this question the salt body with correct shape but 100 $\frac{\mathrm{m}}{\mathrm{s}}$ higher velocity than in the true model is shifted upwards in the starting model. The higher velocity is used to simulate a more realistic situation, as the salt velocity can vary significantly in reality.

The P-wave velocity in the sediment around the salt body is 2000 to 3000 $\frac{\mathrm{m}}{\mathrm{s}}$. With a maximum frequency of 10 Hz the minimum wavelength is 200 m and a theoretical minimum resolution of 100 m can be achieved (see also section 5.1). The FWI was performed for three different vertical shifts:

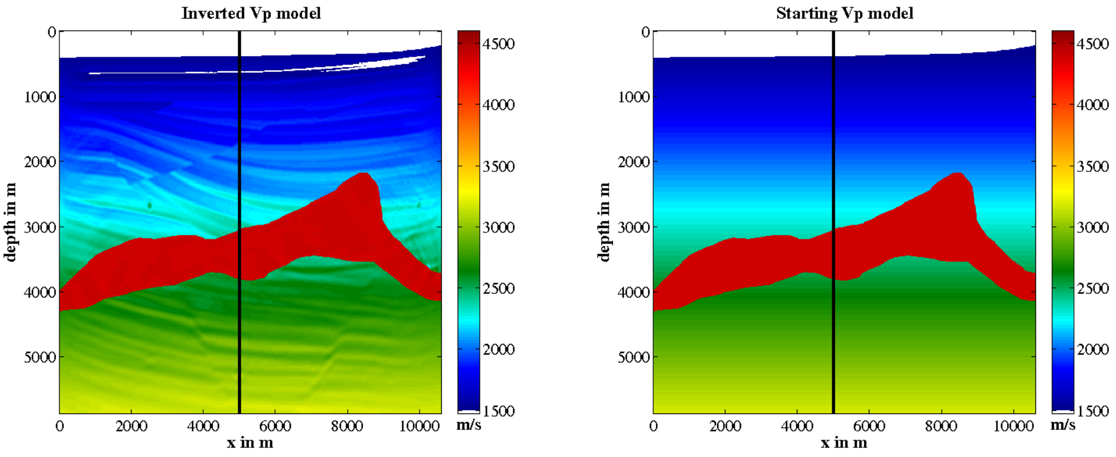

(a) $v_P$ inversion result after 400 iterations.

(b) $v_P$ starting model with salt body.

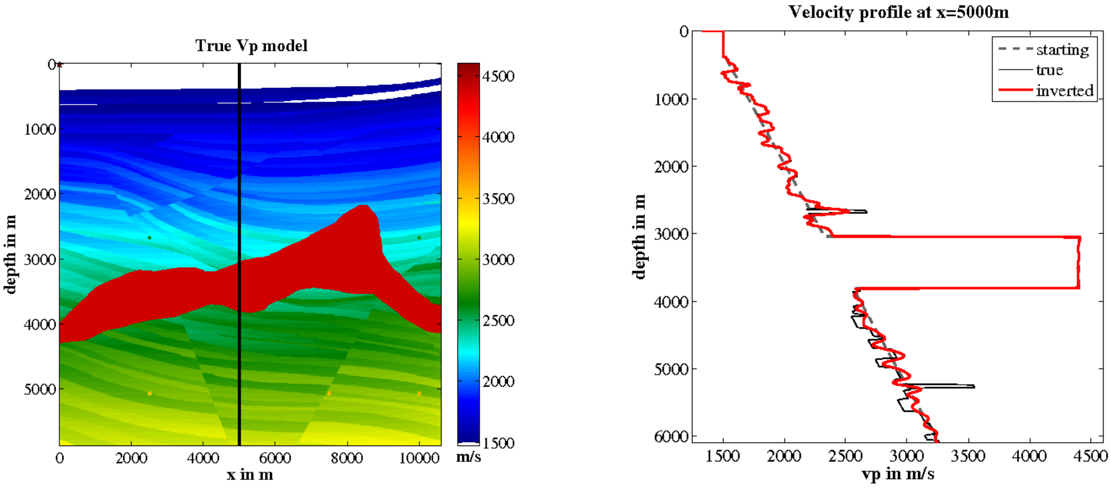

(c) True $v_P$ model.

(d) Velocity profile located at the black line in Figure 5.2a.

Figure 5.2: Test result with salt body at correct location, in correct shape and with correct velocity in starting model.

- 75 m: smaller than the minimum wavelength
- 100 m: equal to the minimum wavelength
- 200 m: two times the minimum wavelength

The left images in Figure 5.4 display the FWI results with the shifted salt body in the starting model. With an increasing shift, more artefacts occur in the FWI results. The plots in Figure 5.5 on the left side show the differences between the FWI results from Figure 5.4 (left side) and the FWI result with the salt body located at the correct position in the starting model (Figure 5.2a). Apparently, the FWI is not able to correct the salt body location. Even the shifts of the salt body by 75 m produces artefacts in the FWI result, mainly in the upper part (Figure 5.4a and 5.5a). The result of the FWI with the shifts of the salt body by 100 m in the starting model (Figure 5.4c and 5.5c) is similar to the result with a 75 m shift. It contains no notable differences. In Figure 5.4e and 5.5e the salt body was shifted upwards by 200 m in the starting model. The artefacts are strongly visible in the upper part of the FWI result. The reason for the artefacts are explained in section 5.2.4.

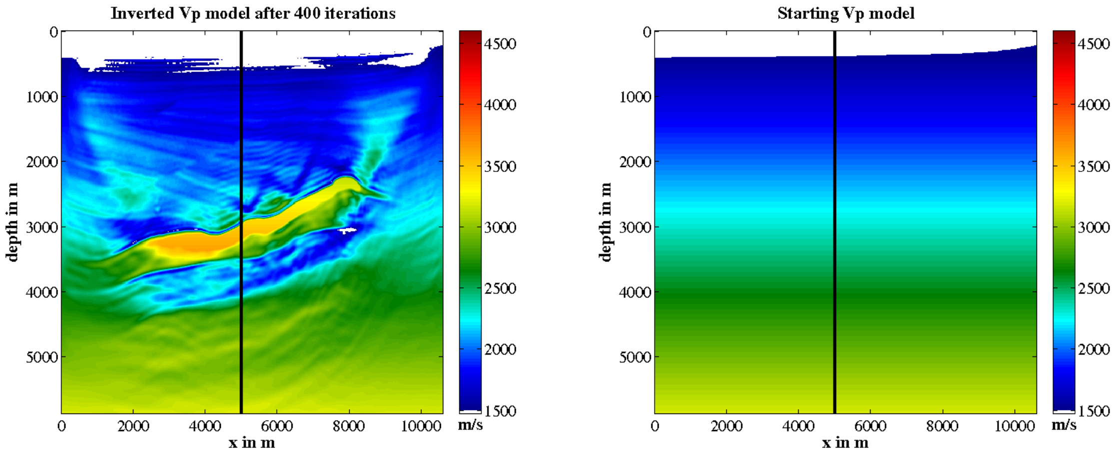

(a) $v_P$ Inversion result after 400 iterations.

(b) $v_P$ starting model with salt body.

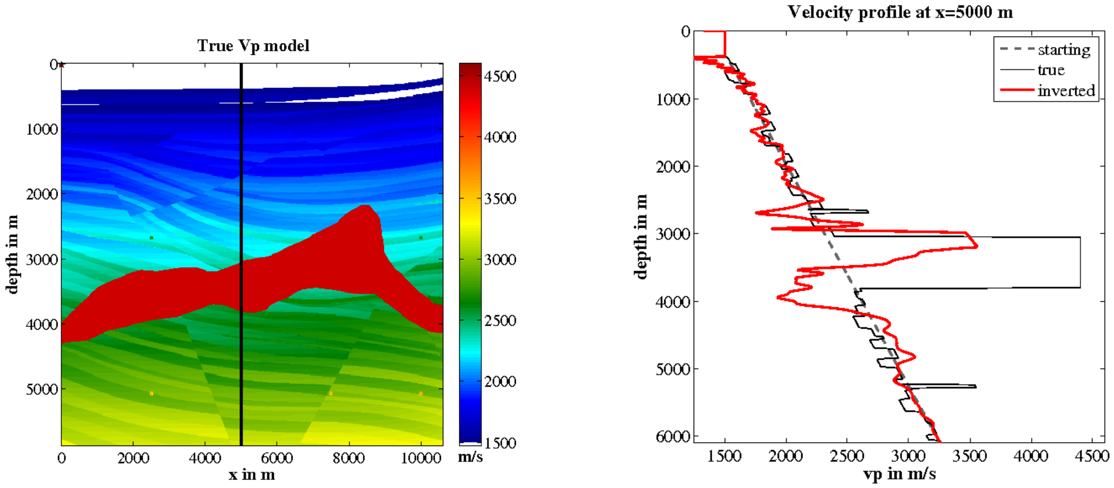

(c) True $v_P$ model.

(d) Velocity profile located at the black line in Figure 5.3a.

Figure 5.3: Test result with no salt body in starting model.

Table 5.1: Relative $v_P$ model error for FWI results in Figure 5.4 for different salt body shifts and different salt-sediment transition zones. The relative model error of the associated starting model is specified in the parentheses.

| | relative model error in % after 400 iterations with | |
|---|---|---|
| salt body shifted up by | hard transition zone | smooth transition zone |
| 75 m | 4.71 (3.88) | 3.60 (3.91) |
| 100 m | 5.95 (4.53) | 4.42 (4.30) |
| 200 m | 9.96 (7.17) | 8.44 (6.76) |

In Table 5.1 the relative model errors (RME) of the FWI results in Figure 5.4 are shown. The RME of the associated starting model is specified in parentheses. The increase of the RME with an increase of the shift is clearly visible as well as the improvement of the result by using a smoothed salt-sediment transition zone. For the 75 m shift of the salt body the RME of the starting model with the smoothed transition zone is worse the value of the hard transition zone. However, the RME of the FWI result with smoothed transition zone is considerably better than with hard transition zone. The RME of the FWI result including the 100 m shift of the salt body in the starting model and the smoothed transition zone is even better than the value of the hard transition zone and the shift of 75 m.

The shifting tests demonstrate the importance of the correct location of the salt in the starting model. Even a small shift by half a minimum wavelength produces artefacts.

### 5.2.4 Cycle Skipping

The reason for artefacts as a consequence of a shifted salt body is the cycle-skipping effect. The FWI code attempts to adapt the modelled data to the field data. For example, the starting model is modified in a way to move a maximum in the waveform of the modelled data to the nearest located maximum of the field data. In case of a sufficiently good starting model the nearest located maximum is the correct maximum resulting from the same structure. If the data of a starting model cannot explain the field data within half a cycle the FWI possibly moves the waveform in a wrong direction. The wrong fitted waveforms result in artefacts in the inverted P-wave velocity model.

As example the 100th trace of the forward modelled seismogram with three different starting models is displayed in Figure 5.6a. The black curve is calculated with a starting model containing the salt body in the correct position. The red trace shows the waveform of the forward modelling with a starting model where the salt body is shifted up by 100 m. The blue dashed line belongs to the modelling with the salt body shifted up by 200 m. When the salt body is shifted up by half a wavelength the extrema are shifted by half a cycle. As a consequence, the FWI can fit the red m1 maximum in the data to the black m1 maximum, or the red m2 maximum to the black m1 maximum. If the salt body is shifted upwards by a full wavelength the FWI will fit the blue m2 maximum to the black m1 maximum. These fits produce artefacts in the resulting model.

To avoid the cycle-skipping effect a sufficiently good starting model is required. One technique to support the correct adaption of the data is analysed in the following section.

### 5.2.5 Salt boundary

To reduce the cycle-skipping effect a blurred transition zone for the sharp sediment-salt interface is inserted in the $v_P$-model. The transition zone is composed of a linear velocity gradient. Half of the transition zone is located in the sediment, the other half in the salt body. Tests with various thicknesses of the transition zone show that the thicker the gradient the more the waveform of the reflection event is pulled apart (Figure 5.6b). The wavelength of a reflection event increases and the amplitude decreases. For a thickness of 500 m the waveforms are reduced to a very low amplitude (about one eighth of the original amplitude). Single reflection events cannot be distinguished anymore. For a transition zone with 250 m thickness both reflection events are clearly visible.

The gradient (250 m thickness) is applied to the starting model containing the shifted salt body. The modelling result is shown in Figure 5.6c. While in Figure 5.6a the red m2 maximum could be fitted to the black m1 or m2, now the red m2 maximum will be fitted most likely to the correct black m2 maximum. Presumably, the blue maxima will still be adapted to the wrong maxima. Hence, a sufficiently smooth transition might improve the outcome of the FWI in case of a small salt body mislocation.

In the following, a linear gradient with a thickness of 250 m is used for the transition zone. The FWI results can be seen on the right side in Figure 5.4 and Figure 5.5. The smooth boundary improves the FWI result. Less artefacts are visible in the velocity models and a better reconstruction around the salt body boundaries is observed. But as the waveforms in Figure 5.6 predicted, a mislocation of a full wavelength cannot be corrected by a gradient during the FWI (Figure 5.4f and 5.5f).

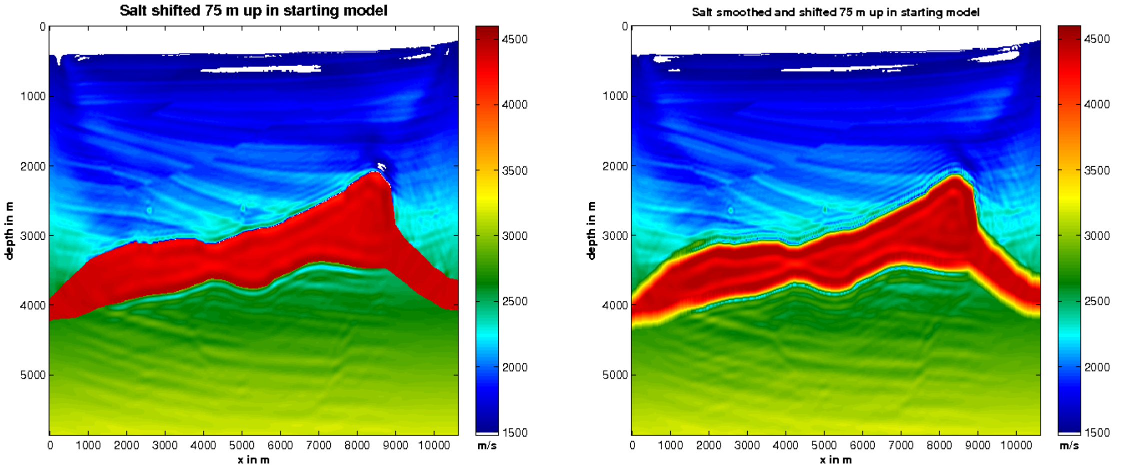

(a) Salt body shifted up by 75 m, hard sediment-salt transition.

(b) Salt body shifted up by 75 m, smoothed sediment-salt transition.

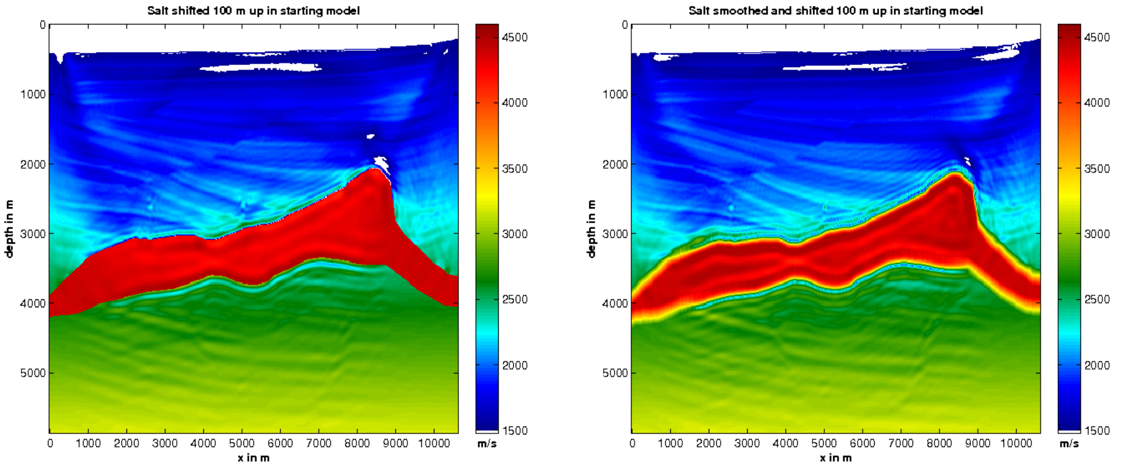

(c) Salt body shifted up by 100 m, hard sediment-salt transition.

(d) Salt body shifted up by 100 m, smoothed sediment-salt transition.

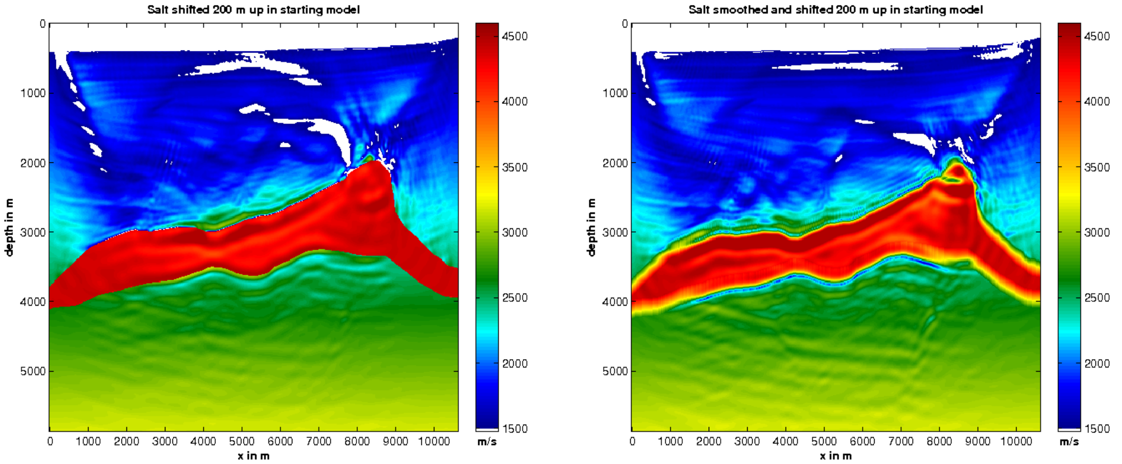

(e) Salt body shifted up by 200 m, hard sediment-salt transition.

(f) Salt body shifted up by 200 m, smoothed sediment-salt transition.

Figure 5.4: Comparisons of FWI results for the $v_P$ model with various shifts of the salt body in the starting models.

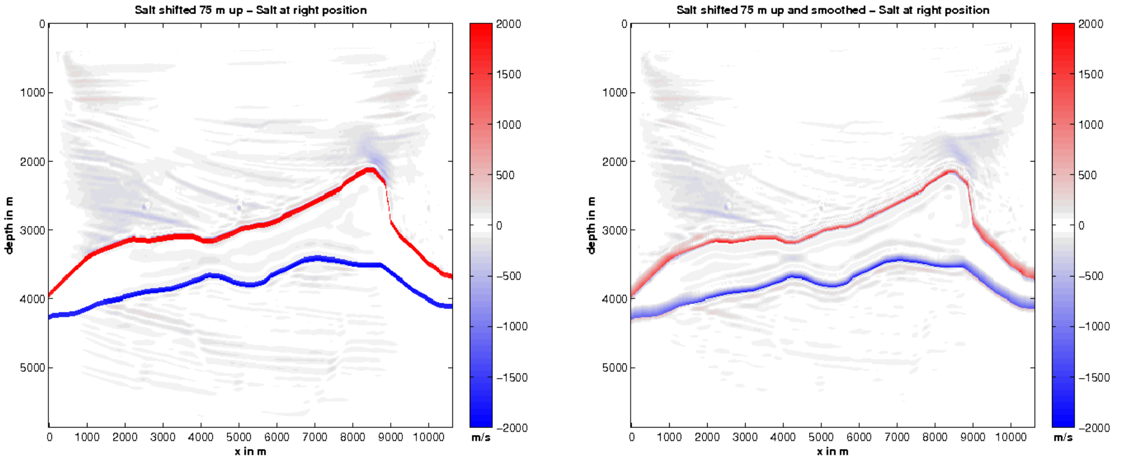

(a) Salt body shifted up by 75 m, hard sediment-salt transition.

(b) Salt body shifted up by 75 m, smoothed sediment-salt transition.

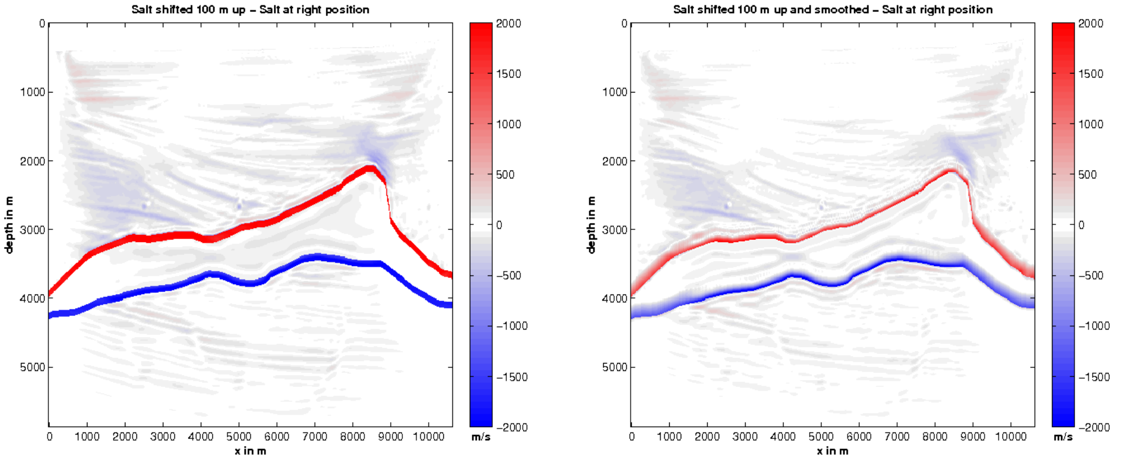

(c) Salt body shifted up by 100 m, hard sediment-salt transition.

(d) Salt body shifted up by 100 m, smoothed sediment-salt transition.

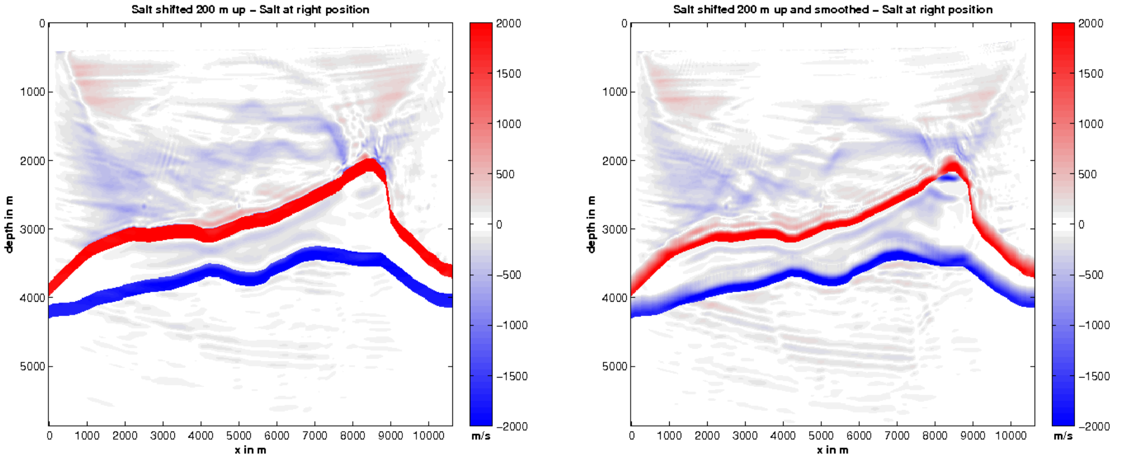

(e) Salt body shifted up by 200 m, hard sediment-salt transition.

(f) Salt body shifted up by 200 m, smoothed sediment-salt transition.

Figure 5.5: Comparisons of FWI results for the $v_P$ model as difference plot (FWI result of a starting model including a shifted salt body minus the FWI result of the starting model including the salt body at the correct location) for differently shifted salt bodies in the starting model.

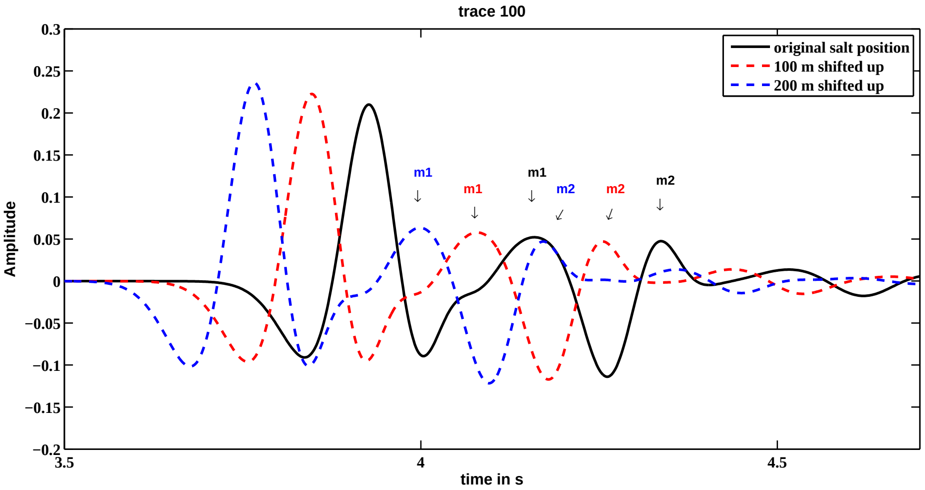

(a) Three different starting models in which the salt body is shifted up.

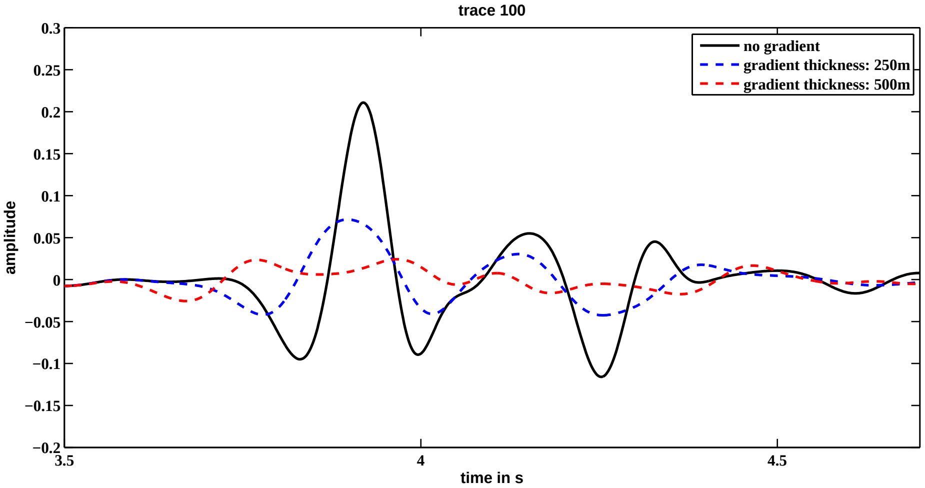

(b) Different gradient thicknesses of the salt-sediment transition.

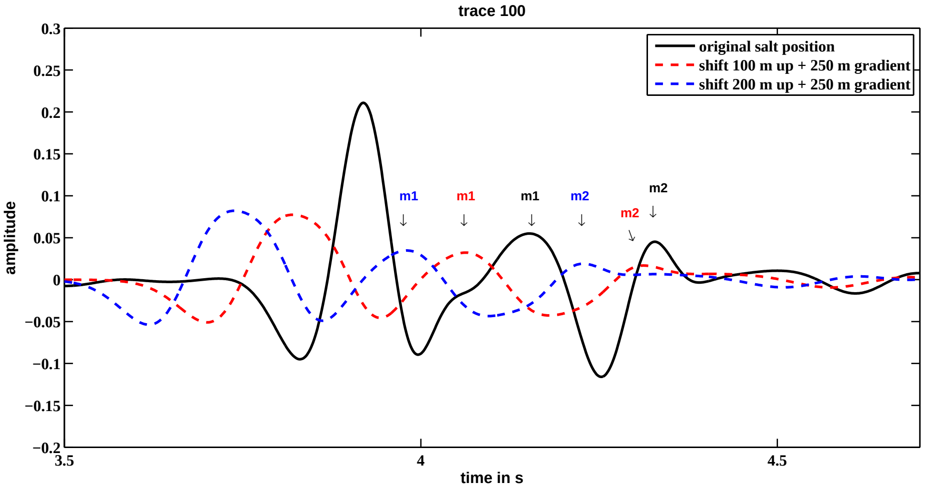

(c) Different shifts with constant gradient of the salt-sediment transition.

Figure 5.6: Trace 100 of the forward modelling for different gradient thicknesses and shifts. Arrows mark the two maxima of the different traces.

## 5.3 Flooding Technique

A promising subsalt imaging technique is the Flooding Technique by Boonyasiriwat et al. (2010). The FWI starts with a very simple velocity model: a 1D linear gradient without any information about the salt body. The first FWI stage is able to reconstruct a rough contour of the top of salt. Everything below this contour line is flooded with salt velocity and used again as starting model. Now the bottom line of the salt body is detected and the space below flooded with a constant sediment velocity. This model is used as starting model for the last FWI to recover the subsalt area.

In the following section the Flooding Technique is used as proposed by Boonyasiriwat et al. (2010) for the acoustic FWI. Due to a suboptimal FWI result, the Flooding Technique was modified in some parts, which is discussed in section 5.3.2. At each iteration the density model is estimated from the velocity model using an empirical relation (Gardner et al., 1974). Therefore, the starting models do not contain any information of the salt body, neither in the density model nor in the velocity model.

### 5.3.1 Original Flooding Technique

The Flooding Technique consists of three FWI stages. The analysis of the misfit curve for 400 iterations of the first FWI stage in Figure 5.7 yields that after 100 iterations all frequencies are included and the misfit does not decrease considerably. To minimise the computational costs the first two stages are performed with only 100 iterations. The third stage is performed using 400 iterations to allow further improvements in the result.

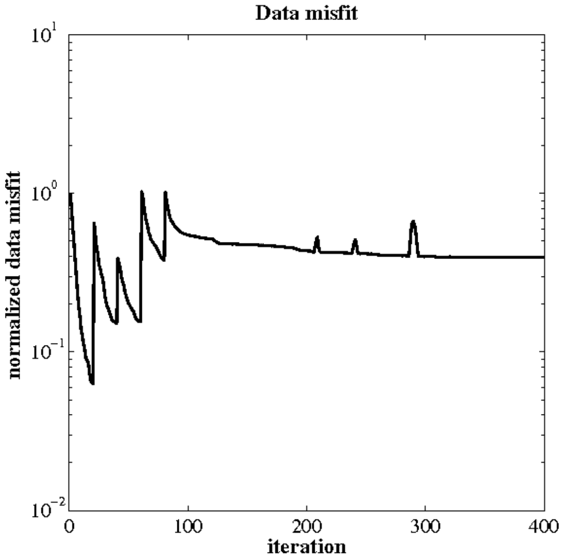

Figure 5.7: Misfit function for the first FWI stage of the original Flooding Technique.

Every FWI stage uses the full 6 s recording time and a 1D linear gradient as starting model (Figure 5.8a). The result of the first FWI stage is shown in Figure 5.8b. Apart from artefacts, the region above the salt body exhibits a satisfactory reconstruction. The top line of the salt body is visible between $x \approx 2000\,\mathrm{m}$ and $x \approx 8000\,\mathrm{m}$. This line is picked automatically via threshold using an external program (own Matlab-script). The boundaries are automatically linearly extrapolated by computing the slope of the last 10 grid points. The threshold needs to be adjusted manually for each test. For this example, the threshold was determined empirically to $2235 - 2250\,\frac{\mathrm{m}}{\mathrm{s}}$. This value is lower than the sediment velocity in this region, but due to a distinctive minimum of approximately $2000\,\frac{\mathrm{m}}{\mathrm{s}}$

just above the top of salt, this was the value with the best results. A careful choice of the threshold enables us to pick the top line at the very small velocity contrast on the right and left edges, too.

The space beneath the picked top salt line is flooded with salt velocity. As we act on the assumption that for field data the exact salt velocity ($v_{\mathrm{P,true}} = 4400\,\frac{\mathrm{m}}{\mathrm{s}}$) is not given or the velocity in the salt body is not constant, a slightly higher velocity ($v_{\mathrm{P,flood}} = 4500\,\frac{\mathrm{m}}{\mathrm{s}}$) is used for the flooding. The resulting starting model for the next FWI stage is displayed in Figure 5.8c.

The FWI result after 100 iterations is shown in Figure 5.8d. In analogy of the procedure after the first stage of the Flooding Technique, the bottom line of the salt body is picked automatically. The contrast of the velocities at the bottom line is much smaller now. The threshold was set to $4450\,\frac{\mathrm{m}}{\mathrm{s}}$. With this threshold the bottom line of the salt was picked in approximately the same x-range as the top line. The line is linearly extrapolated to both sides.

In Figure 5.8e the space beneath the picked bottom line is flooded with the average sediment velocity in this depth ($v_P = 2800\,\frac{\mathrm{m}}{\mathrm{s}}$). In Figure 5.8f the FWI result of the starting model in Figure 5.8e is displayed. The subsalt area contains large-scale structures now and the steeply dipping structures start to become visible.

A more detailed analysis of the FWI result is shown in Figure 5.10. Figure 5.10c displays the difference of the inverted $v_P$ model and the true velocity model. A white colour shows the areas of a perfect match. The difference plot illustrates that the original Flooding Technique detects the top line of the salt body roughly correct. In the middle part between $x = 1000\,\mathrm{m}$ and $x = 9000\,\mathrm{m}$ the maximum location error is $\pm 120\,\mathrm{m}$ in depth direction. Due to the linear interpolation, the edges have a greater error. But, as there is a poor illumination with seismic waves in those parts of the model, the FWI is not affected much. The bottom line is detected very well between $x = 3000\,\mathrm{m}$ and $x = 7500\,\mathrm{m}$. The maximum error in depth direction is $\pm 50\,\mathrm{m}$. Outside of the above mentioned range the location error of the bottom of salt increases due to the linear interpolation.

In Figure 5.10e a velocity profile is shown, located at the black line in Figure 5.10c. In the upper part of the inverted velocity model the sediment layers are reconstructed, but shifted up in comparison to the true model. The salt body has a low velocity anomaly in the middle, which is an attempt of the FWI to correct the salt velocity set too high in the starting model. The subsalt part shows layers, but the absolute velocity cannot be reconstructed if the starting velocity differs too much from the true velocity.

In conclusion, the original Flooding Technique is able to reconstruct the salt body without any a priori information. This technique is limited by the accuracy of the location and shape of the salt body. This results in artefacts in the inverted velocity model (see also section 5.2.3).

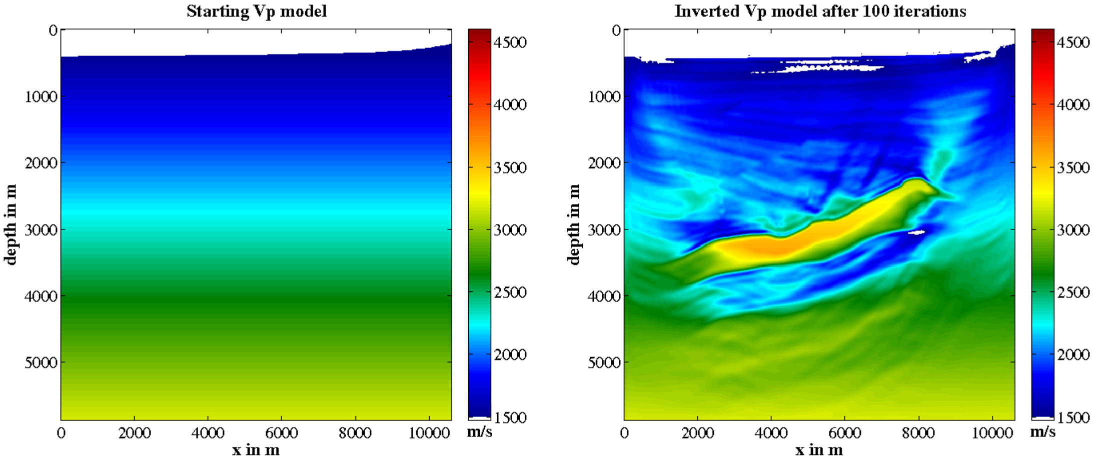

(a) Starting model for the first FWI stage. (b) Result after the first FWI stage.

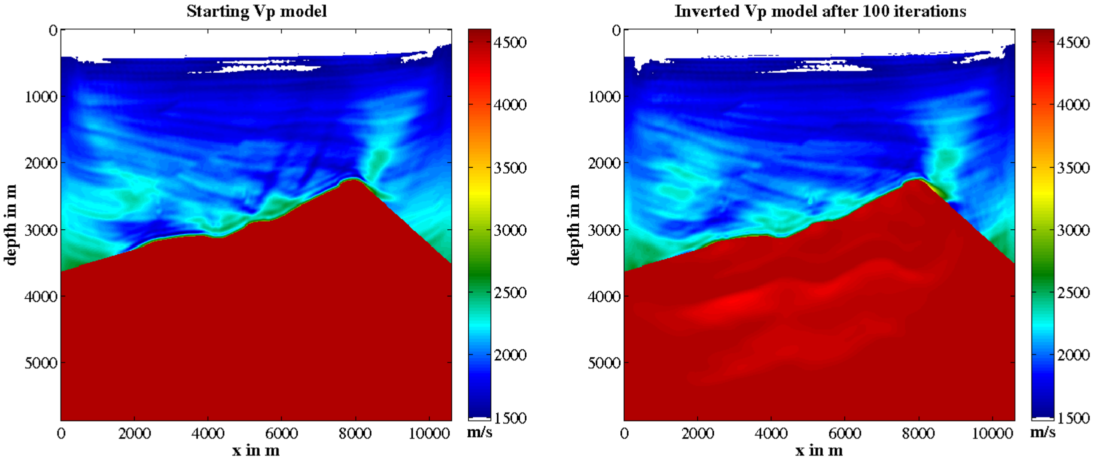

(c) Starting model for the second FWI stage. (d) Result after the second FWI stage.

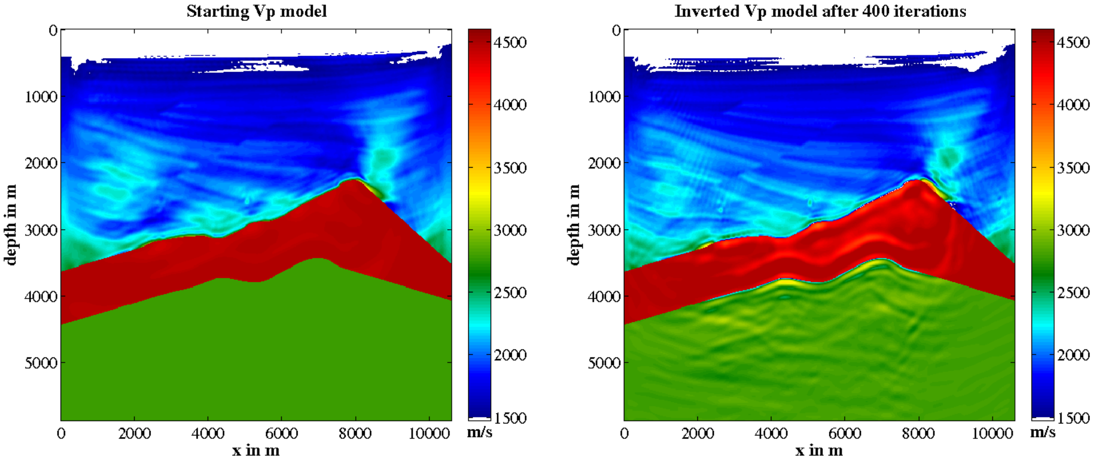

(e) Starting model for the third FWI stage. (f) Result after the third FWI stage.

Figure 5.8: P-wave velocity model at different stages of the original Flooding Technique after Boonyasiriwat et al. (2010).

### 5.3.2 Modified Flooding Technique

In order to reduce the problems and maintain the advantages, the Flooding Technique was modified. Five modifications are introduced and applied in this test:

- a 2D lowpass filter applied to the model,
- the attenuation of pronounced artefacts,
- a smoothed sediment–salt transition zone,
- the flooding with a gradient in the subsalt area,
- and the reconstruction from shallow to deeper parts (time windowing).

Artefacts are suppressed by applying a 2D lowpass filter on the inverted velocity model after every inversion. Small-scale artefacts are reduced and do not affect subsequent inversions. In addition, the very low velocity artefacts directly above the picked top salt line (c.f Figure 5.8c) are removed by overwriting them with the velocity gradient of the first starting model. Due to the high velocity contrast, these are definitely artefacts which can be identified and removed, even if the true velocity model is unknown.

In order to correct small location errors due to the automated picking, a linear gradient as transition zone is introduced in the model after the flooding with salt velocity. The transition zone is located at the top line of the salt body and has a width of 250 m (see also section 5.2.3).

To support the FWI in the subsalt part of the model, the area below the bottom line of the salt body is flooded with a gradient. The advantage in comparison to the flooding with a constant velocity is the more realistic starting model.

The time windowing also reduces artefacts by mitigating the ambiguity of the inverse problem. The increasing amount of data at every iteration stage causes a model reconstruction from shallow parts to deeper parts.

The FWI results are shown in Figure 5.9. The first FWI stage uses the same 1D linear gradient as starting model as the original Flooding Technique (Figure 5.9a). In this stage data with 3 s length are used. These data contain no information of the salt body and reconstruct the area above the salt body (Figure 5.9b). For the next stage data of 4 s length are used. They contain information up to a depth of about 3 km, including the upper part of the salt body. The FWI result is shown in Figure 5.9c. The top line of the salt body is picked as explained in section 5.3.1. The area below the top line is flooded with salt velocity, the gradient is added and the low velocity artefacts are corrected. The model in Figure 5.9d is used as starting model for the third FWI stage. The result after 100 iterations is displayed in Figure 5.9e. Data up to 4.8 s were used for this stage. As a consequence the inverted model contains information about the lower part of the salt body. The bottom line is picked and the sides are extrapolated linearly. Everything below this line is flooded with the same gradient as in the starting model of the first FWI stage (Figure 5.9f). A gradient as transition zone of salt to sediment is not used due to the very good localisation of the bottom line with the original Flooding Technique.

The result of the last FWI stage of the modified Flooding Technique is shown in Figure 5.10b. Less artefacts are visible than in the result of the original Flooding Technique (Figure 5.10a) and the layers in the subsalt area are clearer and better visible. The relative model error of the result obtained by using the modified Flooding Technique displayed in Table 5.2 shows a considerable reduction. In contrast to the difference plot in Figure 5.10c, Figure 5.10d displays a nearly perfect match between the top line of the reconstructed salt body and the top line of the correctly located salt body between $x \approx 1000\,\mathrm{m}$ and $x \approx 9000\,\mathrm{m}$. The bottom line is also reconstructed very well with an error of less than four grid points (50 m) between $x = 0\,\mathrm{m}$ and $x \approx 7000\,\mathrm{m}$. The area above the salt body contains less artefacts. The subsalt part shows a better reconstruction compared with the original Flooding Technique, which is verified by the velocity profiles in Figure 5.10e and 5.10f. The significant improvement is confirmed by the relative model error (RME) displayed in Table 5.2. The RME of the result obtained by the modified Flooding Technique (4.15%) is considerably smaller than the RME of the result obtained by the original Flooding Technique (7.39%).

Table 5.2: Relative $v_P$ model error for the final FWI results obtained by using different Flooding Techniques and different frequency contents. Relative model error of the starting model (Figure 5.9a): 8.91%.

| | relative model error in % after 400 iterations with | |
|---|---|---|
| Flooding Technique | a frequency content of 1-10 Hz | a frequency content of 3-10 Hz |
| modified | 4.15 | 4.42 |
| original | 7.39 | - |

In summary, the results of the FWI using the modified Flooding Technique are clearer, better resolved and closer to the true model than the results obtained using original Flooding Technique. It is possible to reconstruct the salt body very precisely with the modified Flooding Technique without any a priori information about the salt body itself.

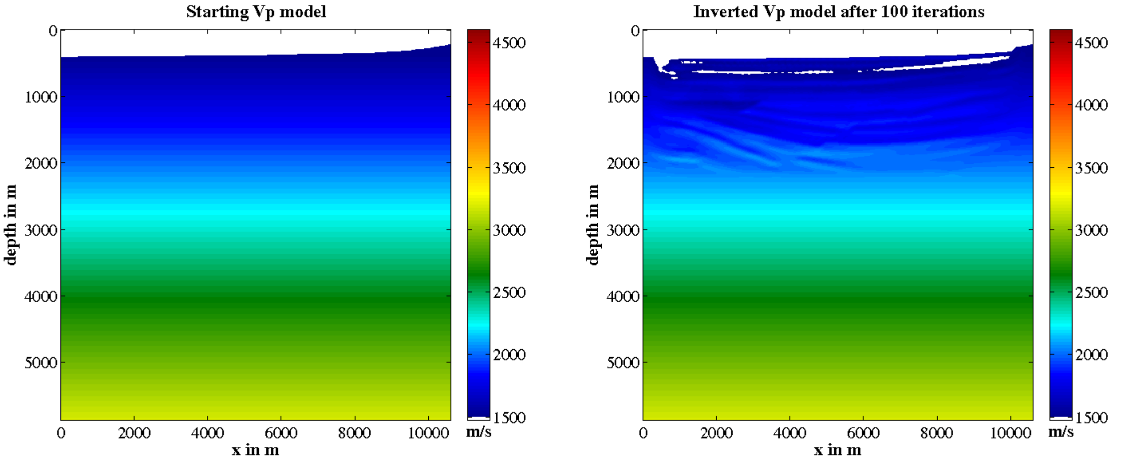

(a) Starting model for the first FWI stage.

(b) Result after the first FWI stage using 3 s long data.

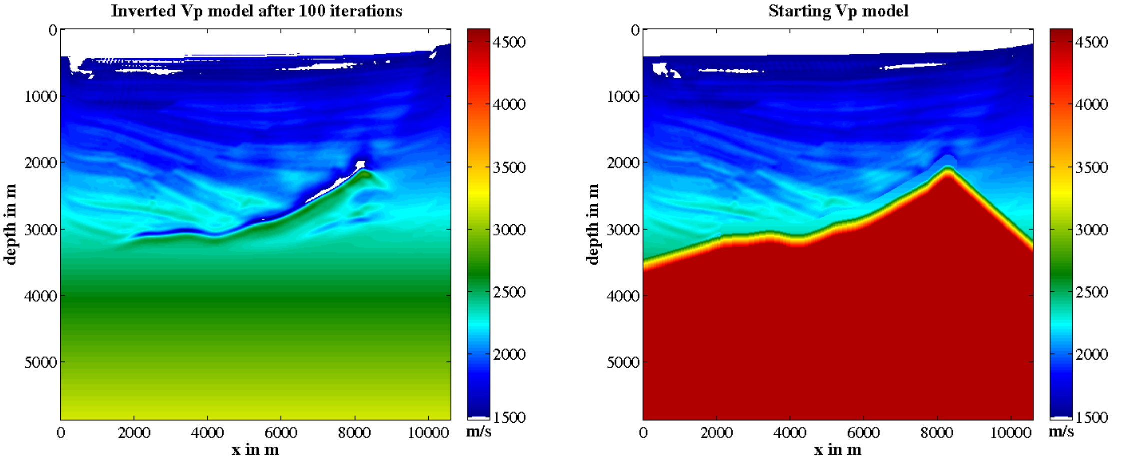

(c) Result after the second FWI stage using 4 s long data.

(d) Starting model for the third FWI stage: corrected artefacts above salt and smoothed transition zone included.

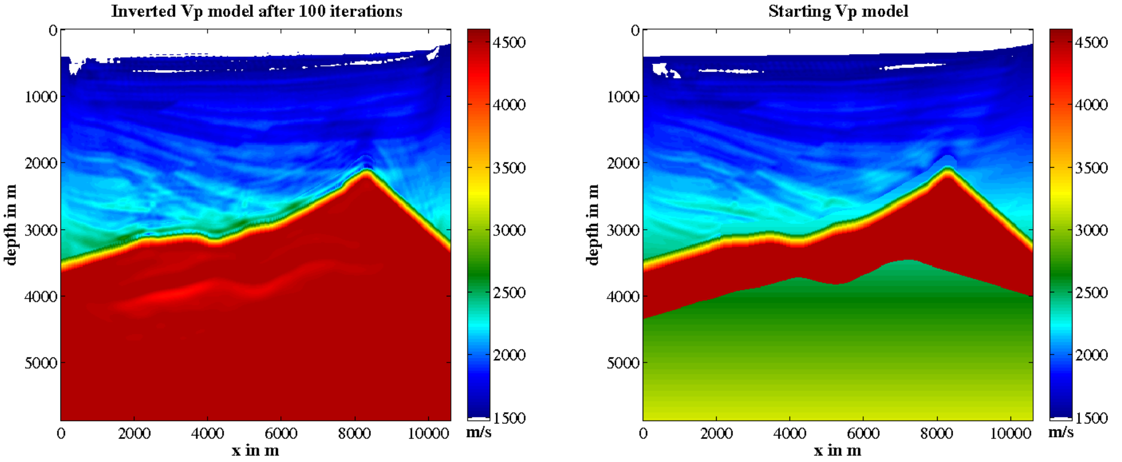

(e) Result after the third FWI stage using 4.8 s long data.

(f) Starting model for the fourth FWI stage: subsalt area is flooded with gradient.

Figure 5.9: P-wave velocity model at different stages of the modified Flooding Technique.

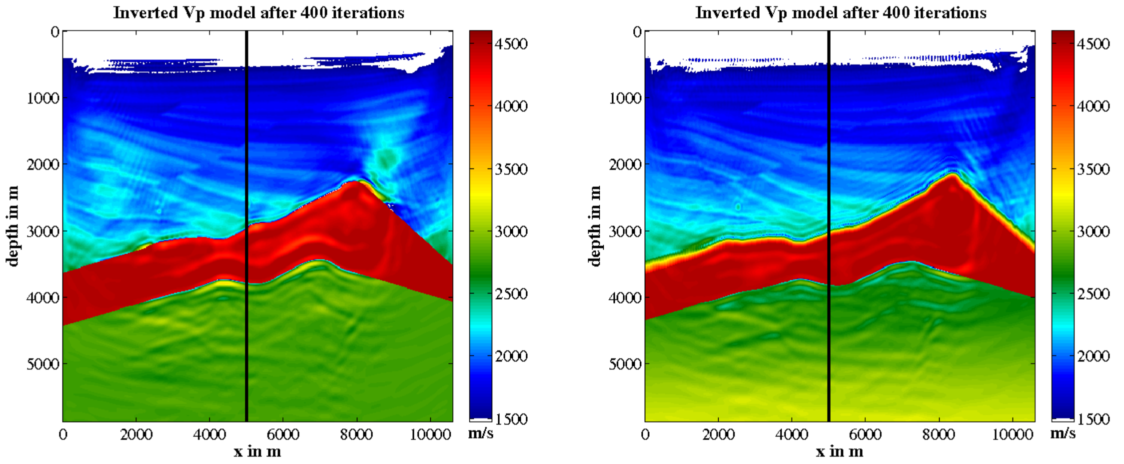

(a) Inversion result after 400 iterations, original Flooding Technique.

(b) Inversion result after 400 iterations, modified Flooding Technique.

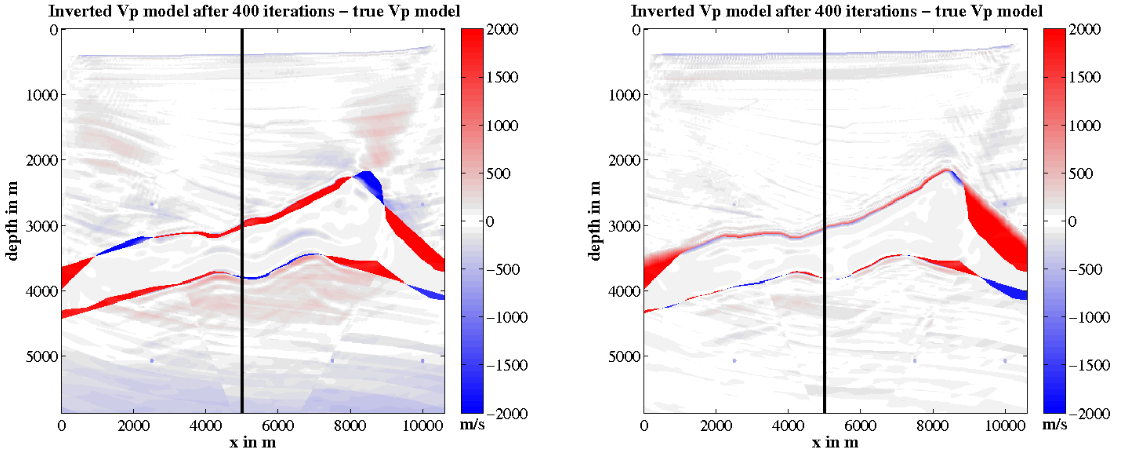

(c) Difference plot: result after FWI minus true model, original Flooding Technique.

(d) Difference plot: result after FWI minus true model, modified Flooding Technique.

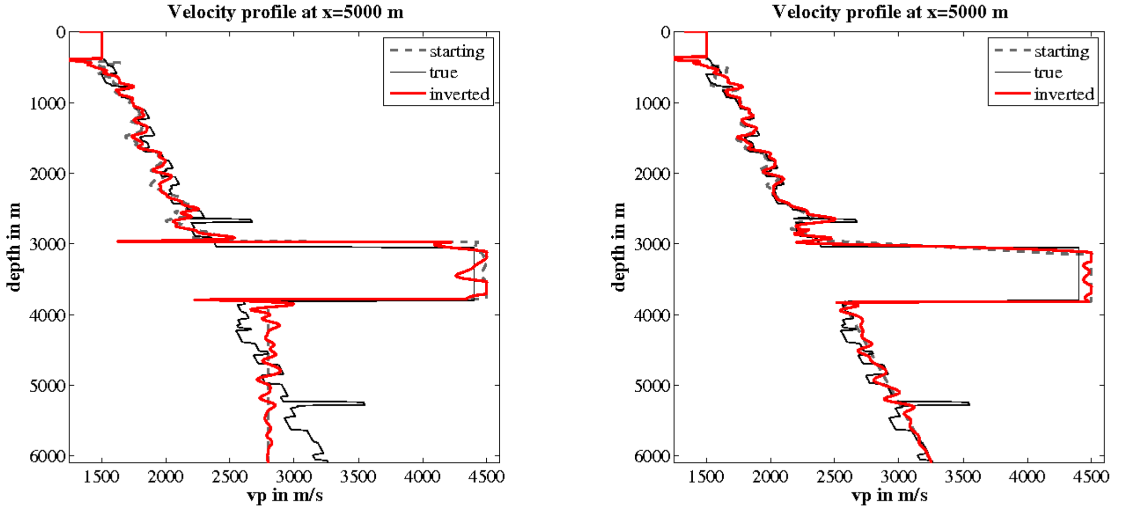

(e) Profile of $v_P$ models located at the black vertical line in Figure 5.10c, original Flooding Technique.

(f) Profile of $v_P$ models located at the black vertical line in Figure 5.10b, modified Flooding Technique.

Figure 5.10: Analysis of the FWI results obtained with the original and modified Flooding Technique.

## 5.4 Frequency content and frequency filtering

The results in section 5.3 were calculated with a frequency content of 1 to 10 Hz. As for the FWI of field data the theoretical minimum usable frequency of broad-band data is approximately 3 Hz, the frequency content for the synthetic modified Flooding Technique was reduced to 3 to 10 Hz and calculated again. The results are displayed in Figure 5.11. The differences of Figure 5.11a and 5.11b are marginal and hardly visible. In Table 5.2 the change of the relative model error is displayed for different frequency contents. The change in the frequency content has no major effect on the RME.

In the FWI frequency filtering is used to reduce the cycle-skipping effect (section 2.2.5 and 5.2.4). It is also used in this work. However, by comparing the results in Figure 7.1a (without frequency filtering) and 7.1c (with frequency filtering) the filtering during the FWI process seems to have no considerable effect on the result as both results are almost identical. Coincidentally, the relative model error of the results with and without filtering have exactly the same value (Table 7.1).

In summary low frequencies are of little importance due to the reconstruction of the salt body by applying the Flooding Technique or involving a sufficiently good starting model. The lack of low frequencies has no considerable effect on the FWI result as well as frequency filtering. However, the frequency filtering is used for all FWIs in this work because it does not affect the FWI negatively and several studies have shown that for worse starting models or a different geometry the frequency filtering is useful (e.g., Bunks et al., 1995; Sirgue, 2006).

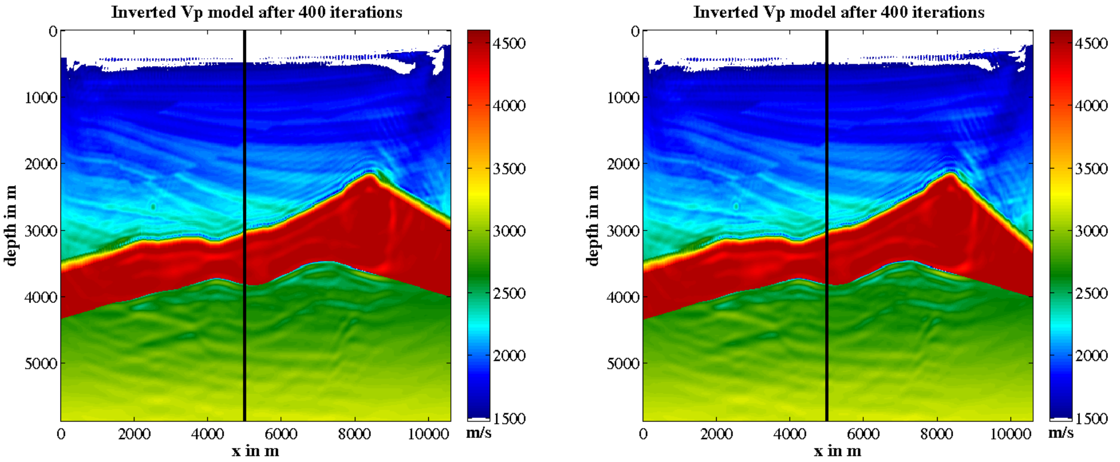

(a) Inversion result after 400 iterations by using the modified Flooding Technique. The data contain frequencies in a range of 3-10 Hz.

(b) Inversion result after 400 iterations by using the modified Flooding Technique. The data contain frequencies in a range of 1-10 Hz.

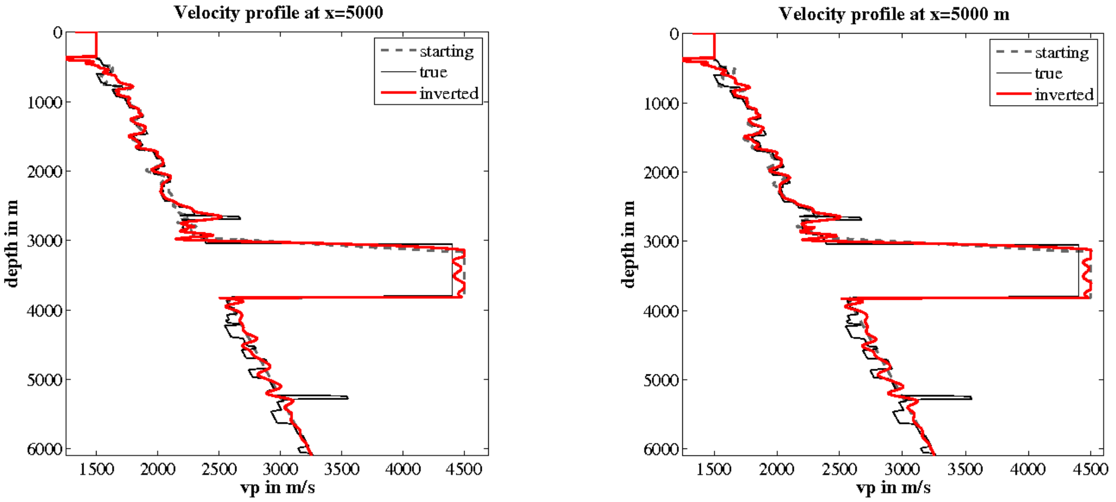

(c) Velocity profile of FWI result in Figure 5.11a.

(d) Velocity profile of FWI result in Figure 5.11b.

Figure 5.11: Analysis of the FWI results obtained with the original and modified Flooding Technique.

# 6. Acoustic FWI with elastic data

The assumption of 2D field data being acoustic is unrealistic. For a more realistic case elastic data are used in the acoustic FWI test described in this chapter. The elastic data differ from the acoustic data due to converted waves. Pure acoustic waves emanated by the source in the water are converted into shear waves at interfaces within the subsurface. After a reflection or refraction in the solid underground the shear waves are converted back into pressure waves at the sea floor. For this reason, the shear waves are recorded indirectly as converted waves. The differences in the wavefield were discussed in section 4.2.

This chapter performs and analyses the results of the acoustic FWI with elastic data. Section 6.1 starts with the optimal starting model including the salt body at the correct location with the correct shape. Section 6.2 investigates the influence of the offset on the FWI result. In section 6.3 the modified Flooding Technique is applied and the results are discussed.

## 6.1 Salt in starting model

The FWI was performed by using the starting model with the 1D velocity gradient as background and the salt body in correct shape and position. The velocity of the salt was set 100 $\frac{\mathrm{m}}{\mathrm{s}}$ higher than in section 5.2.1 for a more realistic scenario. The seismic velocity in salt bodies is usually not exactly known or might be inhomogeneous.

The result of the FWI is shown in Figure 6.1a. The $v_P$ model contains numerous artefacts, especially in the area above the salt body. Large-scale artefacts are located directly above the salt and some smaller festoon-like artefacts between $x = 0\,\mathrm{m}$ and $x = 3000\,\mathrm{m}$, and between $x = 7000\,\mathrm{m}$ and $x = 10625\,\mathrm{m}$.

The FWI tries to explain the elastic data with pure acoustic waves by producing anomalies in the velocity model. By varying the parameters of the FWI the artefacts are reduced. The best result was obtained by using the following parameters:

- normalised L2 norm
- 2D median filter applied to the starting model (filter size: 5 grid points)
- maximum deviation from starting model ($v_P$ and $\rho$) of 20%

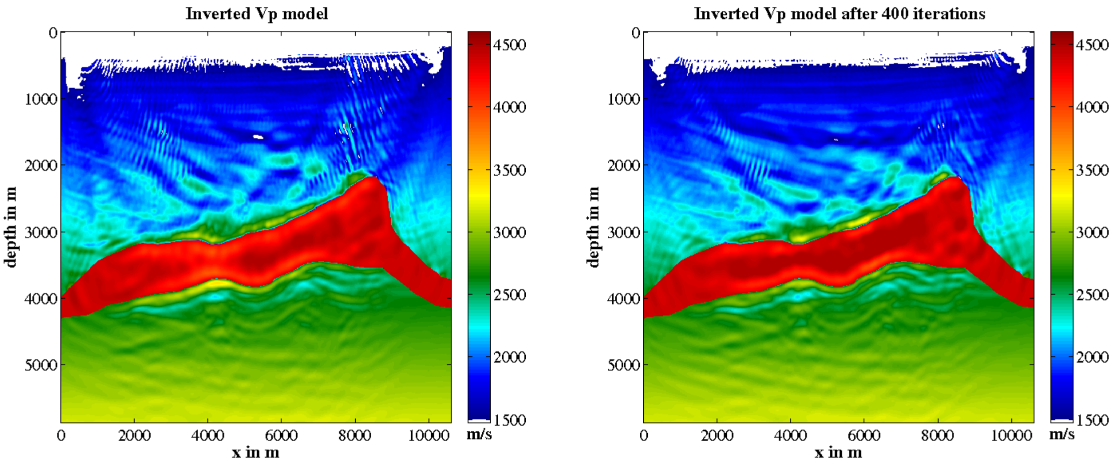

(a) $V_P$ FWI result.

(b) $V_P$ FWI result with modified parameter.

Figure 6.1: Results of acoustic FWI with elastic data and a starting model including a 1D gradient as background model as well as the salt body in correct shape and in the correct location.

In contrast to Figure 6.1a, the amount of artefacts has been reduced (Figure 6.1b). The relative model error is also reduced as shown in Table 6.1.

The first FWI test with elastic data shows the expected problems with artefacts. A variation of the FWI parameters enhances the result slightly. A different approach is the limitation of the offset as discussed in the following section.

## 6.2 Limited offsets

As discussed in section 4.2 the differences in the wavefields of acoustic and elastic data increase with offset. A limitation of the number of receivers used for the FWI is one possible solution to enhance the FWI result. The FWI was performed as explained in section 6.1 by using the modified parameters. The number of receivers was reduced from 751 to 300 and 600. The FWI results are displayed in Figure 6.2 in comparison to the FWI results with the full receiver spread.

The results in Figure 6.2c (600 receivers) and 6.2e (300 receivers) show a considerable reduction of artefacts, which is also noticeable in the relative model error in Table 6.1. However, the resolution of the subsalt part of the model is also reduced. In the velocity profiles in Figure 6.2d and 6.2f the resolution of structures beneath the salt is clearly weaker compared to the FWI result with the full receiver number in Figure 6.2b.

Table 6.1: Relative $v_P$ model error (RME) for the FWI results for different receiver numbers (offset limitation) and different parameter settings (section 6.1). The starting model is displayed in Figure 5.2b (RME: 1.98%).

| | relative model error in % after 400 iterations with | | |
|---|---|---|---|
| FWI parameter | full receiver number (751) | 600 receivers | 300 receivers |
| unchanged | 3.71 | - | - |
| changed | 3.30 | 2.57 | 2.91 |

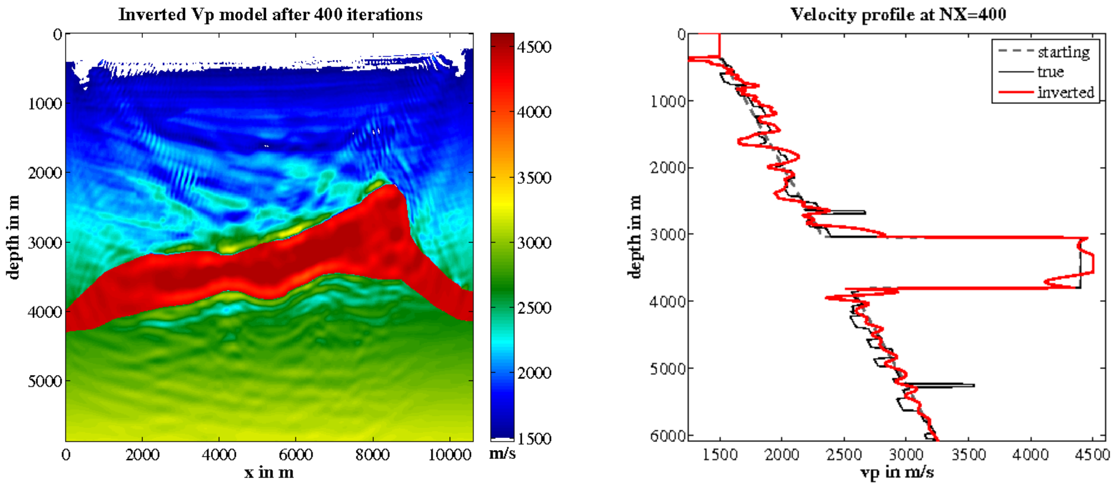

(a) $V_P$ FWI result using the full numbers of receivers.

(b) Velocity profile of of the model in Figure 6.2a at $x = 5000\,\mathrm{m}$.

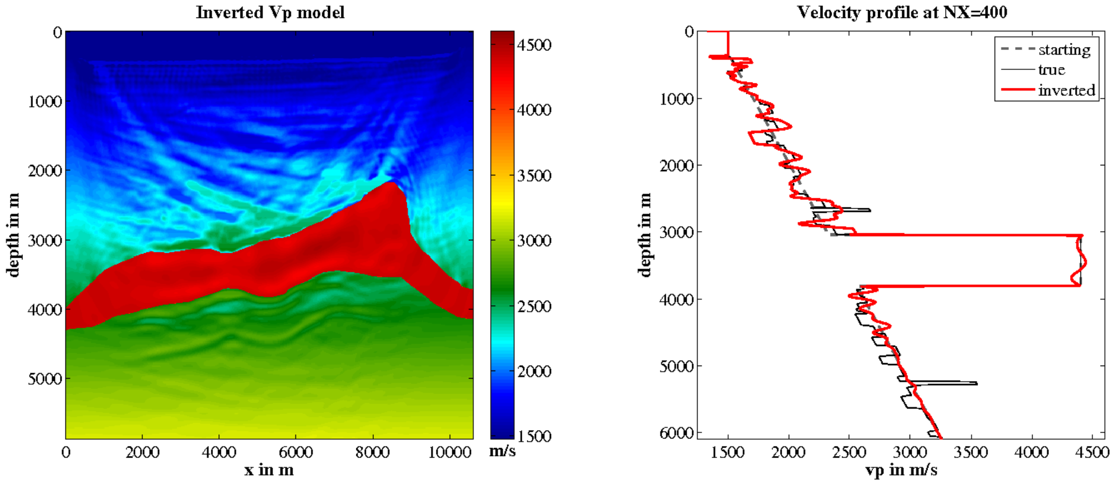

(c) $V_P$ FWI result using 600 receivers.

(d) Velocity profile of the model in Figure 6.2c at $x = 5000\,\mathrm{m}$.

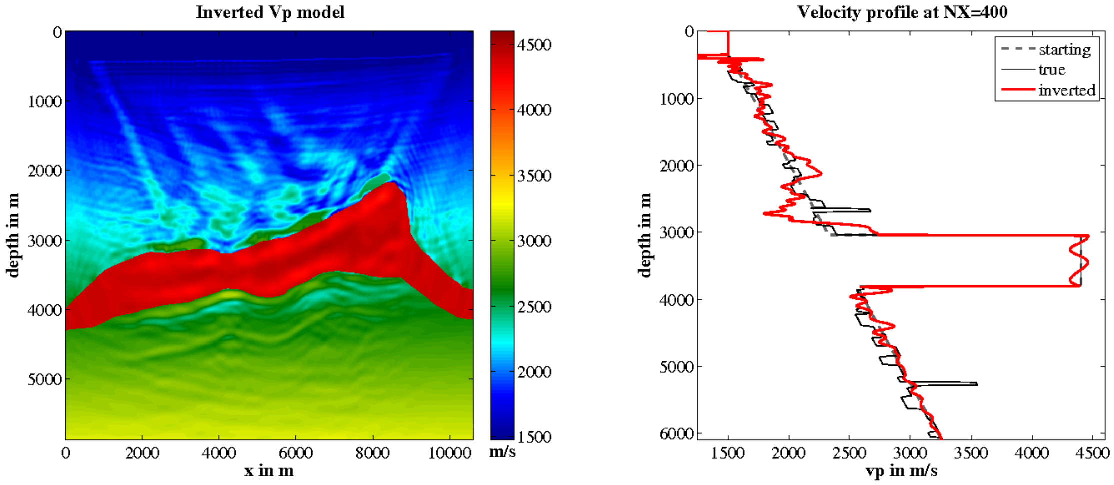

(e) $V_P$ FWI result using 300 receivers.

(f) Velocity profile of of the model in Figure 6.2e at $x = 5000\,\mathrm{m}$.

Figure 6.2: Results for the acoustic FWI with elastic data after 400 iterations with varying number of receiver. The correct salt body was included in the starting model. The FWI parameters were set as declared in the list in section 6.1.

Despite the better relative model error, the limitation of the offset is no solution of the problem because it leads to a considerable reduction of resolution especially in the subsalt area. In the following, the full receiver spread is used.

## 6.3 Flooding Technique

To answer the question if the acoustic FWI with elastic data using the modified Flooding Technique can enhance the result, the modified Flooding Technique is applied as explained in section 5.3.2. The results of the FWI stages and the starting models are displayed in Figure 6.3. The FWI results of the first two stages (Figures 6.3b and 6.3c) are comparable to the FWI results with acoustic data (Figures 5.9a and 5.9b). A closer analysis of the FWI results reveals a reduction of the velocity contrast at the sediment–salt boundary in Figure 6.3c. As a consequence, the linear extrapolations produce different slopes compared to the FWI result with acoustic data. The edges of the salt body are reconstructed worse (cf. Figures 5.10d and 6.4b). The automatic picking is performed in about the same range ($x = 2000\,\mathrm{m}$ to $x = 8000\,\mathrm{m}$).

In preparation for the next stage, the area below the picked top line is flooded with salt velocity. Furthermore, the low velocity artefacts are overwritten with velocities of the starting model. The transition zone is also inserted in the model (Figure 6.3d).

The FWI result of the third stage shown in Figure 6.3e clearly differs from the FWI result in Figure 5.9e. Many large-scale artefacts occur in the area above the top salt line. The reason for the artefacts are differences between the acoustic and elastic data. The differences do not occur in the two previous stages because the differences increase with the length of the time window (cf. section 4.2). However, the algorithm is able to pick a meaningful bottom line of the salt body. Again, it performs an automatic extrapolation at the boundaries. To avoid an influence of the artefacts in the following FWI stages the model in Figure 6.3d is used to create the next starting model and flood the subsalt area with a gradient (Figure 6.3f).

The final result of the last stage of the Flooding Technique with acoustic FWI of elastic data is displayed in Figure 6.4a. The FWI result with the elastic data contains various artefacts as expected. The subsalt area is not resolved very well. Layers are hardly visible and the steeply dipping faults do not exist at all. The difference plot in Figure 6.4b shows a matching top salt line and bottom salt line with the true locations, apart from the extrapolated parts. In contrast to the result of the acoustic data, the extrapolation of the top salt line on the left side does not match with the true location. Furthermore, the gradient of the transition zone is still visible as the FWI could not reconstruct the true location as well as shown in Figure 5.10d. The velocity profile in Figure 6.4c shows mainly the huge artefacts in the velocity model above the salt body and the weak changes from the starting model in the subsalt area.

In summary, the modified Flooding Technique performed with the acoustic FWI with elastic data produces results containing huge artefacts. The structures in the subsalt area are just partially reconstructed.

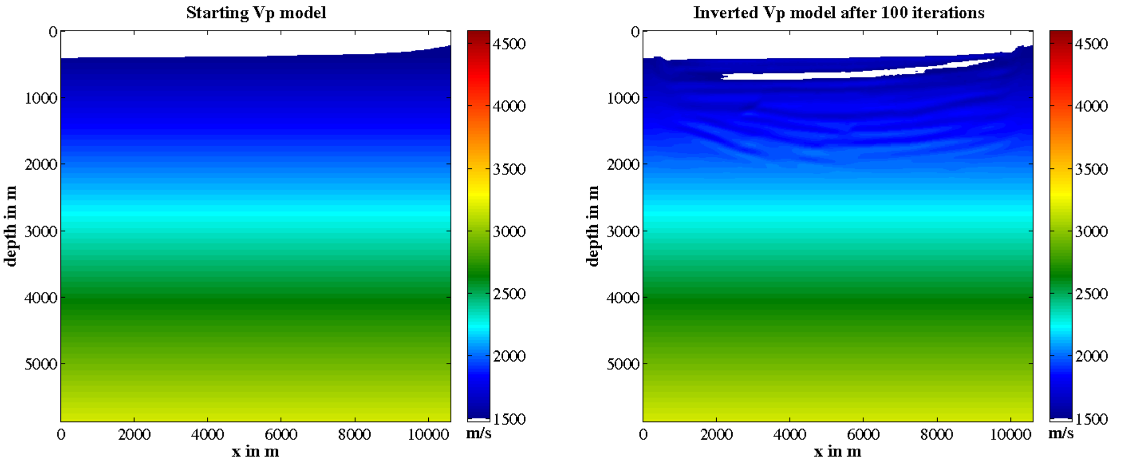

(a) Starting model for the first FWI stage.

(b) Result after the first FWI stage using 3 s of data.

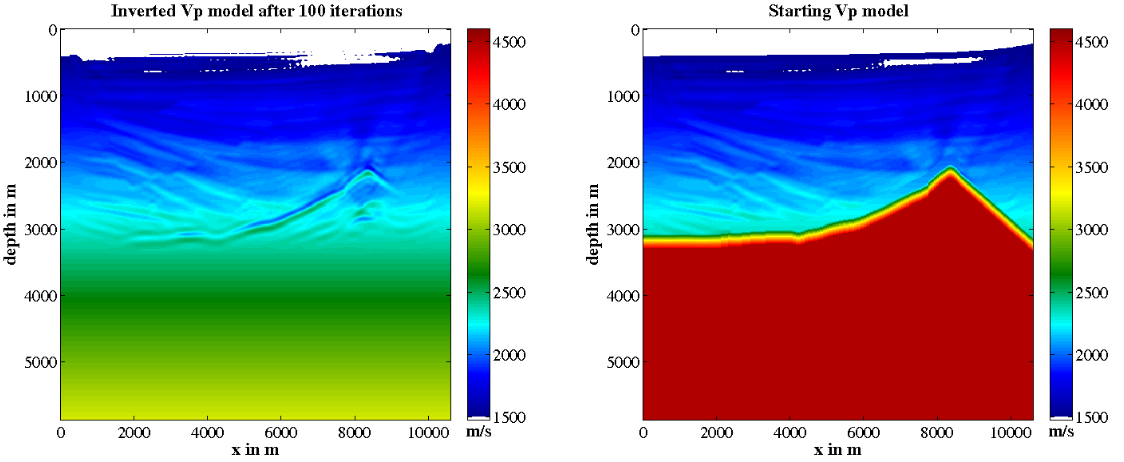

(c) Result after the second FWI stage using 4 s of data.

(d) Starting model for the third FWI stage: corrected artefacts above salt and smoothed transition zone included.

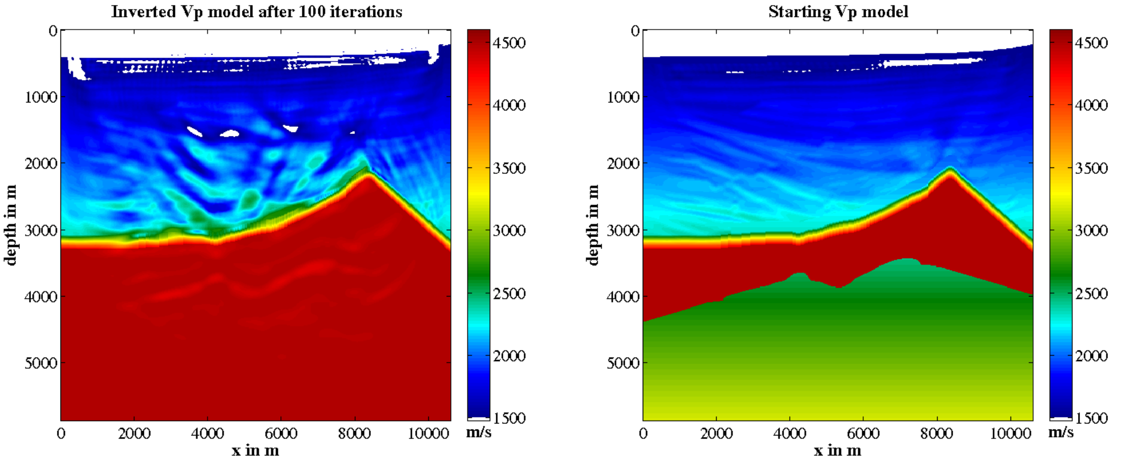

(e) Result after the third FWI stage using 4.8 s of data.

(f) Starting model for the fourth FWI stage: model of Figure 6.3d and subsalt area flooded with gradient.

Figure 6.3: P-wave velocity models at different stages of the modified Flooding Technique using acoustic FWI with elastic data.

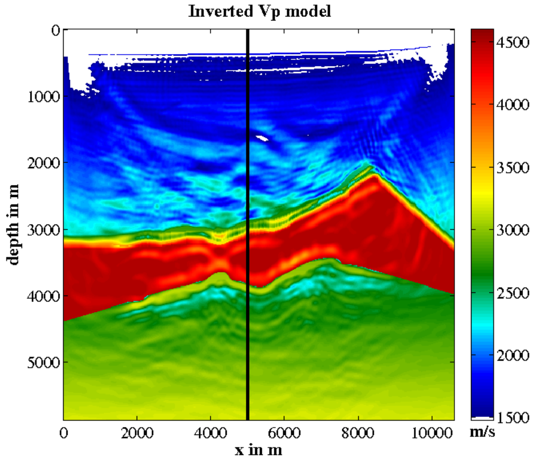

(a) FWI result after 400 iterations.

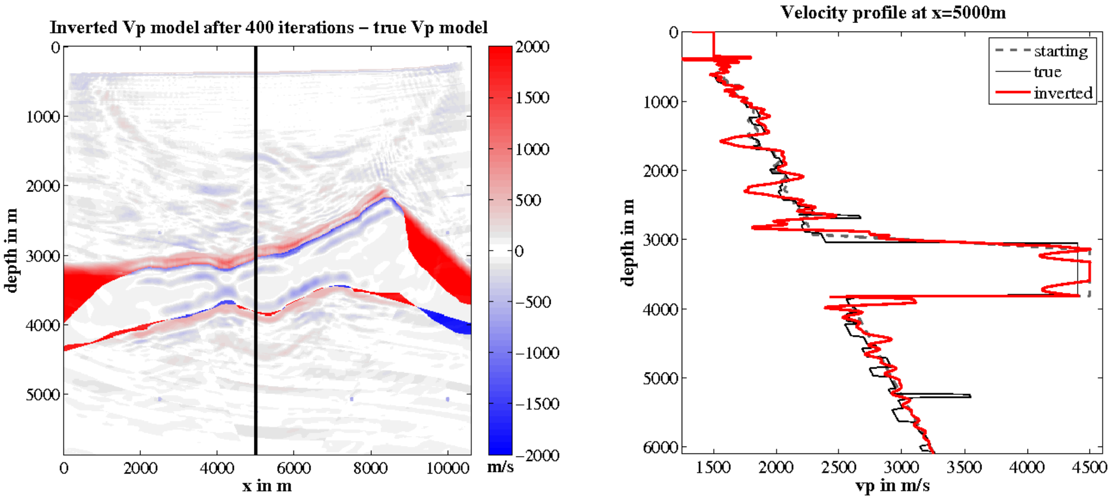

(b) Difference plot: FWI result (Figure 6.4a) minus true model.

(c) Profile of $v_P$ model located at the black line in Figure 6.4a.

Figure 6.4: Analysis of the FWI result obtained by the modified Flooding Technique using acoustic FWI with elastic data.

# 7. Comparison of FWI results with acoustic and elastic data

In this chapter the results of the acoustic FWI with acoustic data (chapter 5) are compared with the results of the acoustic FWI with elastic data (chapter 6). In Figure 7.1 the FWI results are displayed. The structures of the pure acoustic FWI results on the left side are clearly better reconstructed than the results on the right side, obtained by using acoustic FWI with elastic data. The $v_P$ models on the right side contain more artefacts than the models on the left side. By comparing the subsalt area of the Flooding Technique result in Figure 7.1e and 7.1f, the horizontal layers are considerably less visible with elastic data than in the result with acoustic data. The steeply dipping structures are not visible at all and the shape of the left side of the salt body is also not as good as in the result obtained with acoustic data. This observation is also confirmed by the relative model errors (RME) shown in Table 7.1. The RME for the acoustic data is considerably smaller than for the elastic data.

The comparison displays the huge differences in the results of the acoustic FWI by using acoustic or elastic data. Both the FWI with a very good starting model (section 6.3) and the Flooding Technique (section 6.1) produce models containing a considerable amount of artefacts using elastic data. One possible solution is the elastic FWI, introduced and applied in the next chapter.

Table 7.1: Comparison of the relative $v_P$ model error for the acoustic FWI results with acoustic and elastic data.

| | relative model error in % after 400 iterations | | |
|---|---|---|---|
| acoustic | salt in starting model | | modified |
| FWI with | no frequency filtering | with frequency filtering | Flooding Technique |
| acoustic data | 1.63 | 1.63 | 4.65 |
| elastic data | 2.35 | 3.71 | 6.44 |

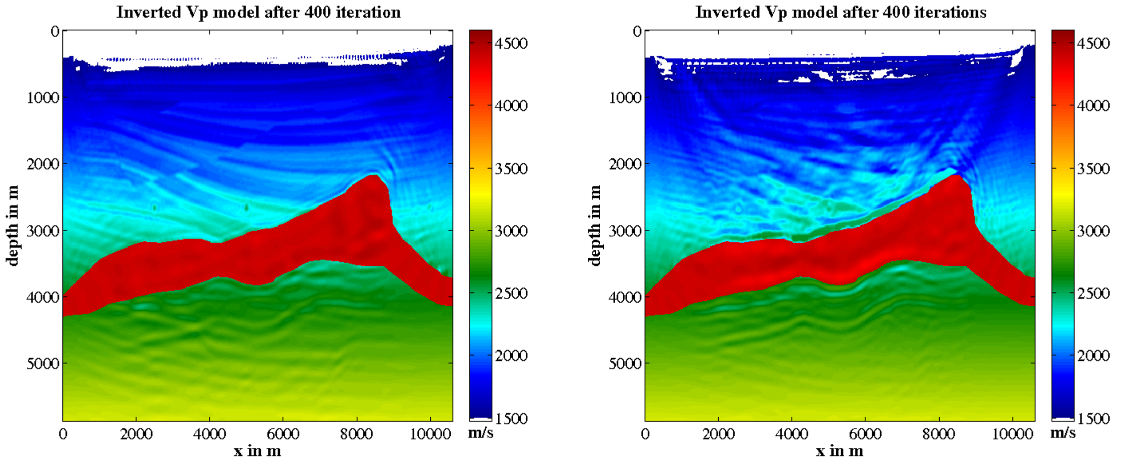

(a) FWI result using acoustic data with salt in starting model without frequency filtering.

(b) FWI result using elastic data with salt in starting model without frequency filtering.

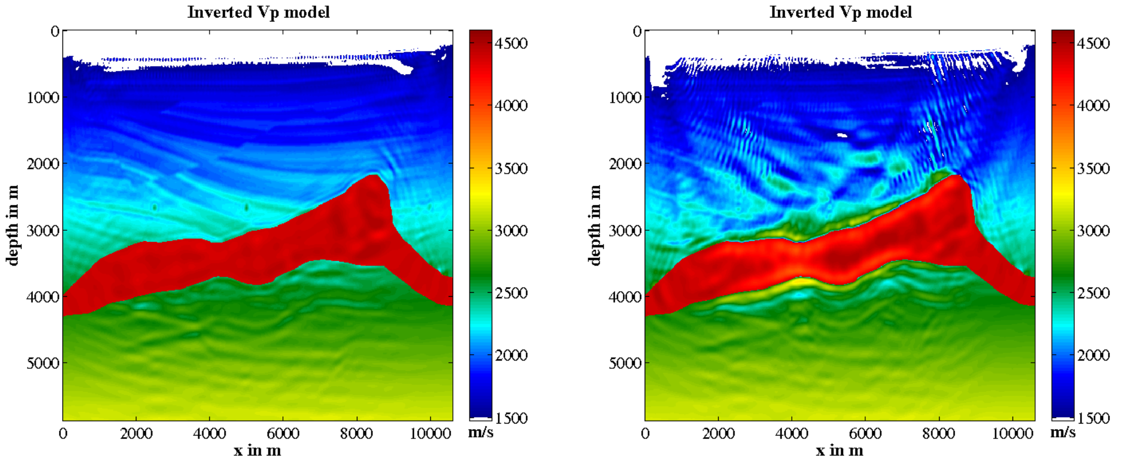

(c) FWI result using acoustic data with salt in starting model with frequency filtering.

(d) FWI result using elastic data with salt in starting model with frequency filtering.

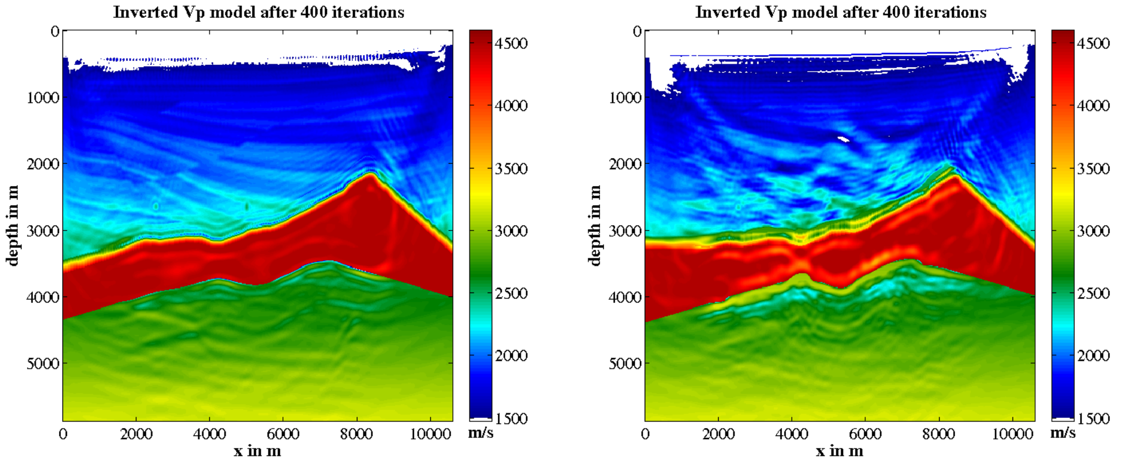

(e) Modified Flooding Technique with acoustic data.

(f) Modified Flooding Technique with elastic data.

Figure 7.1: Analysis of the FWI results after 400 iterations obtained by acoustic FWI with acoustic and elastic data (frequency content: 3-10 Hz).

# 8. Elastic FWI with elastic data and comparison with the acoustic FWI

The elastic inversion was performed by DENISE (section 2.2.7). The results of the acoustic and elastic FWI are comparable with limitation due to the different gradient calculation. The acoustic code is based on pressure, while the elastic on particle displacement (cf. section 2.2.3).

The elastic FWI was performed for the $v_P$ and the $v_S$ models, the true density model was given. The starting models contain a 1D linear gradient as background model and the true salt body. A frequency filtering was not used due to technical problems.

The results for $v_P$ and $v_S$ of the elastic FWI after 38 iterations are shown in Figures 8.1e and 8.1f. For comparison the acoustic FWI was computed without frequency filtering using the same starting models. The results of the acoustic FWIs after 40 and 100 iterations are shown in Figures 8.1a to 8.1d.

A comparison of the acoustic FWI result with acoustic data and the elastic FWI shows great similarity. Both FWIs converge in the same number of iterations to a similar $v_P$ model result. The velocity profile in Figure 8.2a emphasises this. The black and red lines match almost perfectly. Only small differences occur in the subsalt part and the diffraction points in a depth of about $y = 5200\,\mathrm{m}$ are not reconstructed due to the lack of high frequencies in this area.

The relative model errors of the inverted models are also very similar for both FWIs (Figure 8.3b). The elastic FWI just converges a little faster than the acoustic FWI. For the elastic FWI the relative model error is about 0.04% smaller than for the acoustic FWI after 40 iterations. The relative model errors are also displayed in Table 8.1. The misfit of the data in the elastic FWI decreases strictly over all iterations (Figure 8.3a). Due to flattening of the data misfit, this curve crosses the curve of the data misfit of the pure acoustic FWI at iteration 15. The flattening produces a break of the FWI at iteration 38. This stop criterion takes effect when the decrease in the data misfit is too small.

The model error of the acoustic FWI of elastic data shows a different behaviour. In the first seven iterations the model error decreases down to about 1.8%. Structures above the salt body starts to appear in the model (Figure 8.4a and 8.4b). For later iterations the relative model error increases again. At iteration 25 the relative model error even surpasses

Table 8.1: Comparison of relative $v_P$ model error of acoustic and elastic FWI.

| | | relative model error in % | | |
|---|---|---|---|---|
| FWI | data | after 40 iterations | after 100 iterations | starting model |
| acoustic | acoustic | 1.38 | 1.24 | 1.98 |
| acoustic | elastic | 2.11 | 2.66 | |
| elastic | elastic | 1.34 | - | |

the value of the starting model. In Figure 8.4c the FWI result after 14 iterations is shown where the RME in Figure 8.3b shows a kink. Some artefacts can now be seen. In contrast to the model error, the data misfit decreases at every iteration with few exceptions (blue line in Figure 8.3a).

In summary, the elastic FWI result for the $v_P$ model is comparable to the result of the acoustic FWI with acoustic data. The $v_S$ result in Figure 8.1f shows just weak updates in the upper part of the model above the salt body. Large-scale structures starting to appear in the updated model. The relative model error increases strictly up to 2.13% at iteration 38.

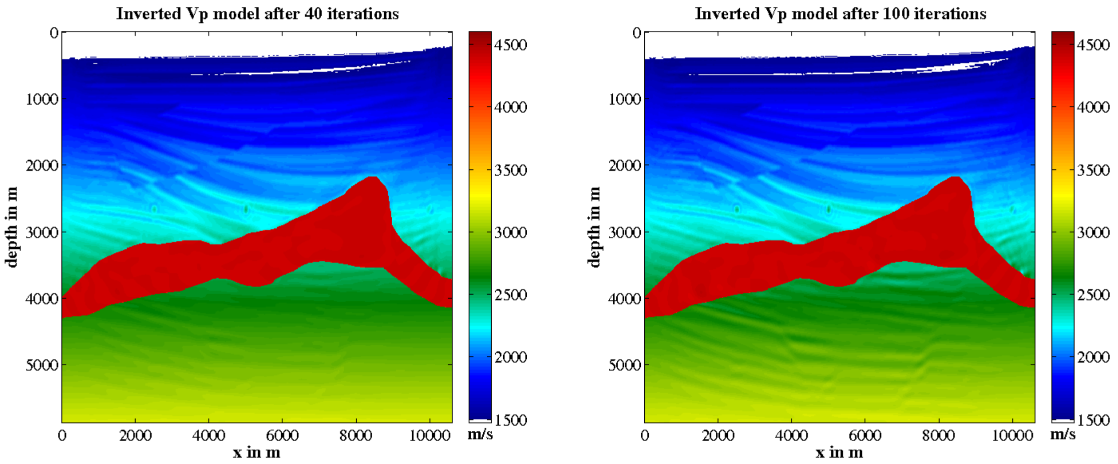
Inverted Vp model after 40 iterations

Inverted Vp model after 100 iterations

(a) $V_P$ model after acoustic FWI with acoustic data (after 40 iterations).

(b) $V_P$ model after acoustic FWI with acoustic data (after 100 iterations).

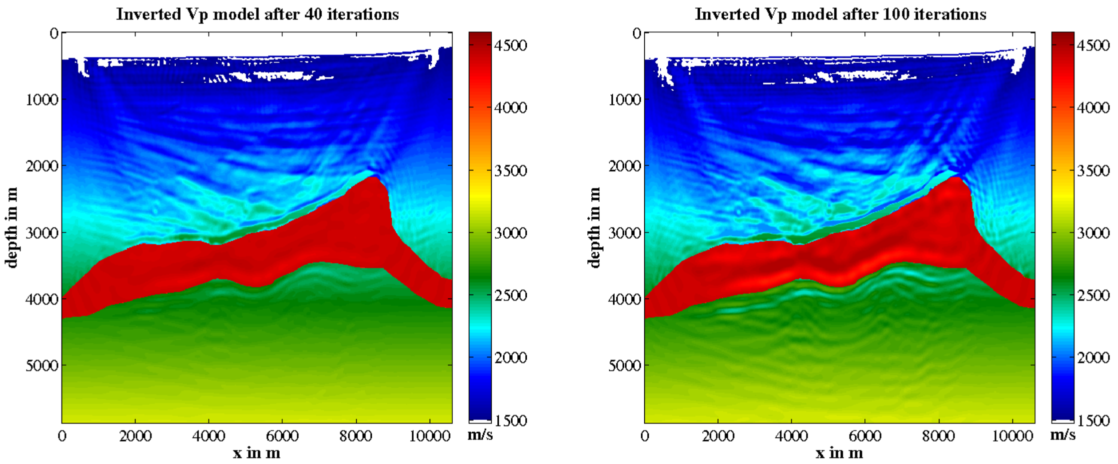
Inverted Vp model after 40 iterations

Inverted Vp model after 100 iterations

(c) $V_P$ model after acoustic FWI with elastic data (after 40 iterations).

(d) $V_P$ model after acoustic FWI with elastic data (after 100 iterations).

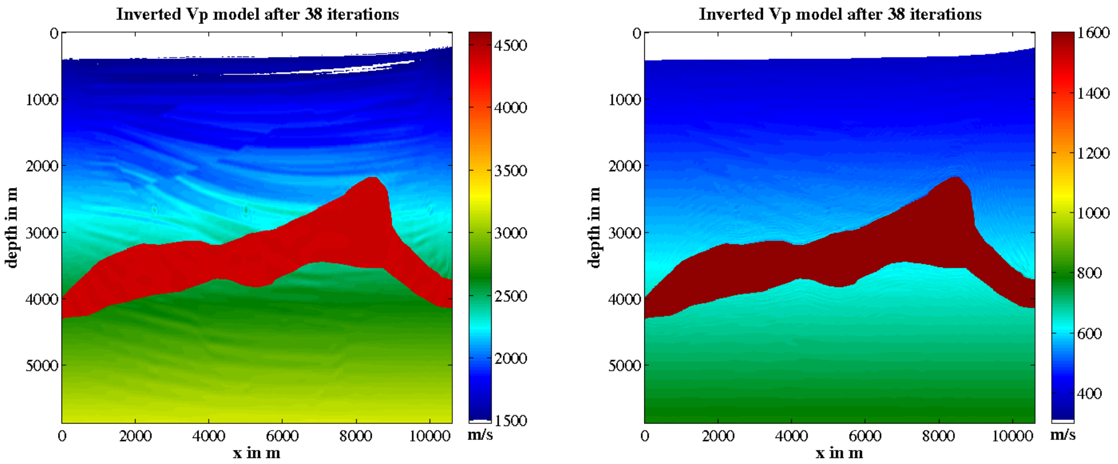
Inverted Vp model after 38 iterations

Inverted Vp model after 38 iterations

(e) $V_P$ model after elastic FWI with elastic data (after 38 iterations).

(f) $V_S$ model after elastic FWI with elastic data (after 38 iterations).

Figure 8.1: Comparison of the results of the acoustic and elastic FWI with acoustic and elastic data (no frequency filtering; true density model).

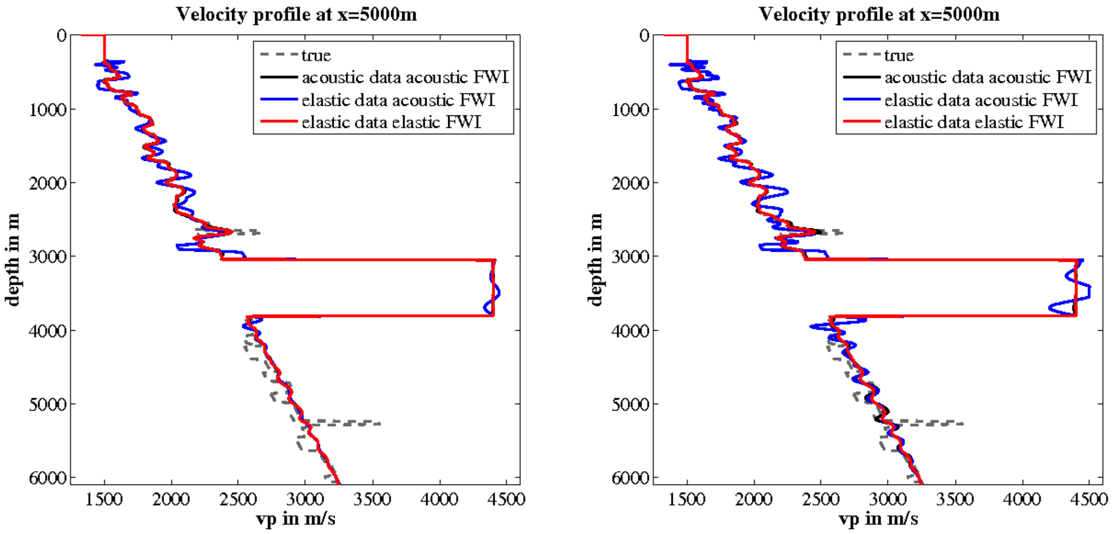

(a) After 40 iterations (elastic FWI after 38 iterations).

(b) After 100 iterations (elastic FWI after 38 iterations).

Figure 8.2: Comparison of the results of the acoustic and elastic FWI with acoustic and elastic data (velocity profiles) shown in Figure 8.1.

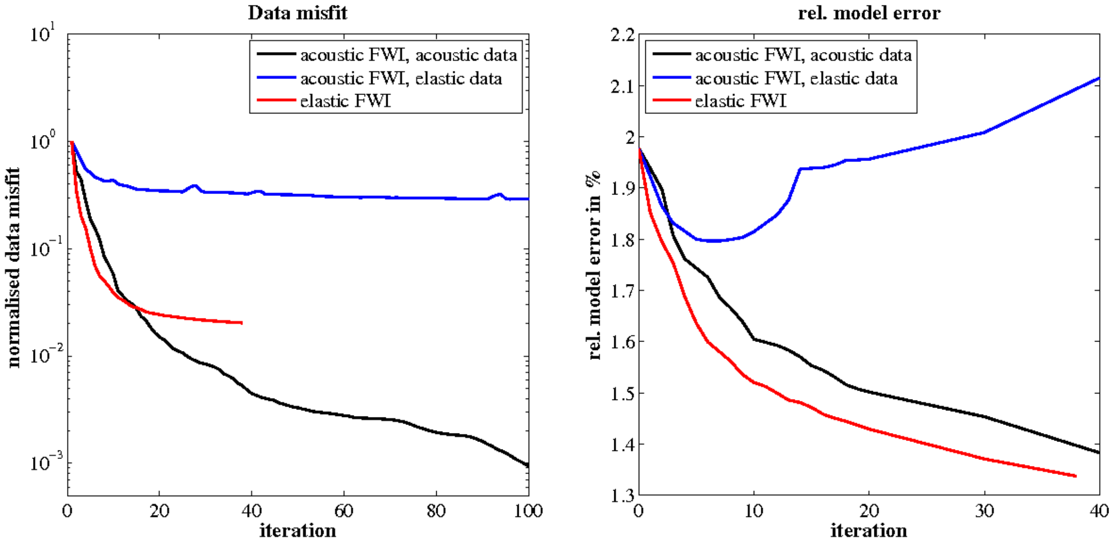

(a) Data misfit during the FWI.

(b) Model error of the FWI result for the $v_P$ model relative to the true model.

Figure 8.3: Data misfit and relative model error of the FWI results shown in Figure 8.1.

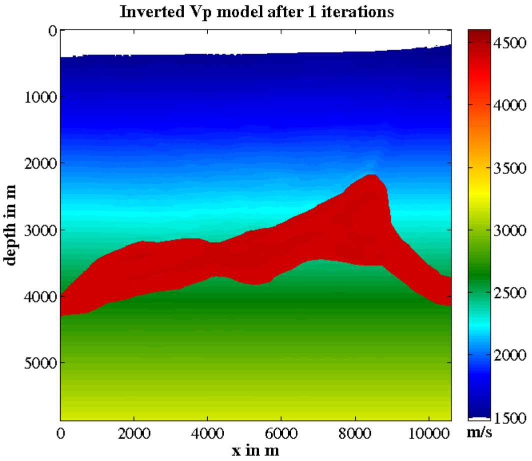

(a) After first iteration.

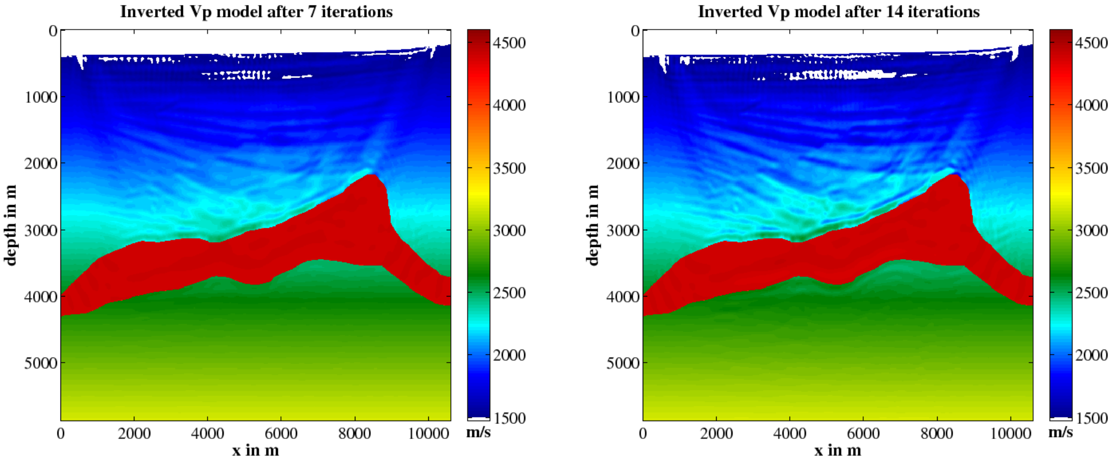

(b) After seventh iteration.

(c) After 14th iteration.

Figure 8.4: P-wave velocity results of the acoustic inversion with elastic data (no frequency filtering; true density model).

# 9. Summary and conclusion

In this work I applied the Full Waveform Inversion (FWI) in the time domain to the problem of subsalt imaging and developed a modified Flooding Technique. Differences relevant for the FWI of acoustic and elastic data were discussed and solutions for several problems developed.

### Model description and acquisition geometry

For the synthetic FWI studies reference models are required (section 3.1). The $v_P$ model was created by using a subpart of the migration velocity model delivered by Fugro and has a size of about 10.5 km in x-direction and 6 km in depth. The velocity gradient of the background was replaced by a subpart of the Sigsbee2A model, constructed for the Gulf of Mexico, also representing the origin of the field data (section 3.1.1). The $v_S$ and density models were calculated from the $v_P$ model (section 3.1.2 and 3.1.3). The acquisition geometry is based on the real acquisition geometry with a large offset of 9.5 km (section 3.3).

### Forward modelling

In section 4.1 synthetic seismograms were calculated by using models including different structures. The structures were assigned to events in the seismograms for a better understanding of the wave propagation and the complex wavefield, especially for events resulting from subsalt structures. The study demonstrated the problem of subsalt imaging for conventional methods because the low amplitude events coming from the subsalt area overlap each other and are not distinguishable.

For the FWI studies elastic and acoustic data were used. To get an idea of the difference and possible problems occurring during the FWI the elastic and acoustic data were compared and analysed in section 4.2. The differences in the tests are considerable and vary with offset. The differences in the data increase with the offset up to 5-7 km on the x-profile, then decrease again, reaching the level of misfit of the first 2 km at 8-9 km. Due to converted waves, the differences exist in spite of a marine acquisition geometry and shear waves are recorded indirectly. The amount of converted wave energy depends on the incident angle, in which the waves hit the sediment-salt boundary.

### Acoustic inversion with acoustic data

The checkerboard test in section 5.1 was the first test of acoustic FWI with acoustic data. By perturbing the true velocity model with a chequerboard-like pattern the FWI result gives information about the resolution of different parts in the model for a given acquisition geometry. The chequerboard pattern above the salt body is well resolved. In the subsalt part of the model the chequerboard pattern is visible but not resolved as well as it is in the upper area. The test gave an idea of the resolution in the model for the subsequent FWI tests. It is possible to resolve structures in the subsalt area.

In a test the required quality of the starting model for a successful inversion was studied (section 5.2). By using a one-dimensional linear gradient as background model and the correct salt body in the correct location in the starting model, the true model is reconstructed very well by the acoustic FWI with acoustic data (section 5.2.1). The entire model is reconstructed almost perfectly. All sedimentary layers and steeply dipping structures in the subsalt part are resolved. This example shows the large potential of the FWI pertaining to the subsalt imaging problem.

If the starting model contains no information of the salt body the FWI fails (section 5.2.2). Only a rough estimate of the top salt line is reconstructed and the upper part of the model contains numerous artefacts. In the subsalt part no structures are reconstructed. Apparently, more information about the salt body are required to perform a successful FWI. To estimate the required accuracy of these information the salt body was shifted up in the starting model (section 5.2.3). This study shows that even a shift of the salt body smaller than one wavelength (75 m) produces artefacts in the resulting model. The number of grows with an increase of the shift, especially in the upper part of the model, produced by the cycle-skipping effect. The number of artefacts is reduced for small displacements (up to one wavelength) of the salt body by introducing a transition zone at the sediment-salt boundary.

To avoid the requirement of precise a priori information for the salt body the Flooding Technique (Boonyasiriwat et al., 2010) was applied (section 5.3). The Flooding Technique is a multi-stage inversion strategy reconstructing the model in three stages:

- first stage: FWI with a starting model without salt body
- second stage: picking the top line of the salt body in the model result of the first stage and flooding the area below with salt velocity before applying the FWI
- third stage: picking the bottom line of the salt body in the model result of the second stage and flooding the area below with sediment velocity before applying the FWI

In the result of the Flooding Technique the salt body is reconstructed with a location error of 50-75 m. The edges of the salt body have a greater error due to the linear extrapolation. The poor matches at the model edges do not influence the remaining part of the model notably because of the poor illumination and therefore a low information content of these parts in the data. A few artefacts are visible but considerably less than in the FWI with the mislocated salt body in the starting model. In the subsalt part the thicker layers are reconstructed and the steeply dipping structures started to get visible.

A small location error of the salt body is one possibility to enhance the imaging result in the subsalt part. Therefore, the original Flooding Technique was modified:

- a 2D lowpass filter applied to the model,
- the attenuation of pronounced artefacts,

- a smoothed sediment–salt transition zone,
- the flooding with a gradient in the subsalt area,
- and the reconstruction from shallow to deeper parts (time windowing).

In the result of the modified Flooding Technique the upper part of the model contains almost no artefacts. The location error of the salt body is below 50 m, apart from the model edges including the extrapolations. The layers in the subsalt are also better resolved than in the result of the original Flooding Technique. The FWI adapts the velocities in the layers to the real velocity and not only relative velocity changes.

The modified Flooding Technique produces realistic FWI results by reconstructing the salt body without any a priori information about the salt body. The last stage of the modified Flooding Technique reconstructs the layers and faults in the subsalt area very well.

### Acoustic FWI with elastic data

A more realistic approach is the usage of elastic data. The acoustic FWI is the fastest approach with relatively low computational cost. Therefore, the acoustic FWI is tested as described in this chapter 6. As expected, the acoustic FWI with elastic data produces results containing many artefacts. The artefacts are the result of the attempt to explain the elastic data with acoustic modelling. By varying the parameters of the FWI the artefacts are reduced but not completely avoided. In the subsalt area, only the thicker layers are reconstructed. The steeply dipping structures are not visible.

As the differences of the acoustic and elastic wavefields increase with offset, a limitation of the offset was analysed. The use of only 600 receivers improves the result considerably. Less artefacts are visible and the relative model error decreases by almost one percent down to 2.57%. By using 300 receivers the FWI result is also improved visually but the RME is 0.3% higher than with 600 receivers. The disadvantage is the clear impact on the resolution in the subsalt area. The data recorded by the long offset receivers contain important information of the subsalt area. Therefore, a limitation of the offset is no solution for the problem of acoustic FWI with elastic data.

The modified Flooding Technique produces results with a large amount of artefacts. The salt body is not constructed as precisely as with acoustic data. Structures in the subsalt area are reconstructed only partly.

### Elastic inversion with elastic data

The acoustic FWI of elastic data does not reconstruct the subsalt area successfully. Therefore, the elastic FWI was applied on the elastic data (chapter 8). First tests show comparable results for the elastic FWI and the acoustic FWI of acoustic data. The results are visually identical and the relative model error is very similar. Another advantage is that we obtain a $v_S$ model in addition. A successful FWI on $v_P$ and $v_S$ waves delivers important information of fluid or gas reservoirs in the subsalt area. The first elastic FWI over only 40 iterations produces a $v_S$ model with weak updates. Some structures are visible in the upper part above the salt body. Further iterations will probably lead to a better $v_S$ model result.

### Conclusion

This work shows the large potential of the FWI for the problem of subsalt imaging. The acoustic FWI, especially with the modified Flooding Technique, produced good results. The differences of acoustic and elastic data are considerable. Due to these differences the result of the acoustic FWI of elastic data for the subsalt imaging problem is not applicable. On the contrary, the first tests with elastic FWI were very successful. The next step would be to apply the modified Flooding Technique with elastic FWI, followed by the application to field data.

# Bibliography

Aki, K. and Richards, P. G. (1980). *Quantitative Seismology: Theory and Methods.* A series of books in geology. Freeman, San Francisco.

Bohlen, T. (2002). Parallel 3-D viscoelastic finite difference seismic modelling. *Computers & Geosciences*, 28(8):887–899.

Boonyasiriwat, C., Schuster, G. T., Macy, B., Valasek, P., and Cao, W. (2010). Application of multiscale waveform inversion to marine data using a flooding technique and dynamic early-arrival windows. *Geophysics*, 75(6):R129–R136.

Bunks, C., Saleck, F. M., Zaleski, S., and Chavent, G. (1995). Multiscale seismic waveform inversion. *Geophysics*, 60(5):1457–1473.

Chauris, H., Noble, M., and Taillandier, C. (2008). What initial velocity model do we need for full waveform inversion? In *Extended Abstracts, 70th EAGE Conference & Exhibition.*

Choi, Y. and Alkhalifah, T. (2012). Application of multi-source waveform inversion to marine streamer data using the global correlation norm. *Geophysical Prospecting*, 60:748–758.

Collino, F. and Tsogka, C. (2001). Application of the perfectly matched absorbing layer model to the linear elastodynamic problem in anisotropic heterogeneous media. *Geophysics*, 66(1):294–307.

Courant, R., Friedrichs, K., and Lewy, H. (1928). Über die partiellen Differenzengleichungen der mathematischen Physik. *Mathematische Annalen*, 100(1):32–74.

Courant, R., Friedrichs, K., and Lewy, H. (1967). On the partial difference equations of mathematical physics. *IBM journal of Research and Development*, 11(2):215–234.

Cox, R. A., Culkin, F., Greenhalgh, R., and Riley, J. (1962). Chlorinity, conductivity and density of sea-water. *Nature*, 193:518–520.

CREWES Zoeppritz Explorer Applet (24. September 2013). CREWES, the consortium for research in elastic wave exploration seismology. `http://www.crewes.org/ResearchLinks/ExplorerPrograms/ZE/ZEcrewes.html`.

Gardner, G. H. F., Gardner, L. W., and Gregory, A. R. (1974). Formation basics for velocity and density - the traps diagnostic stratigraphic. *Geophysics*, 39(6):770–780.

Komatitsch, D. and Martin, R. (2007). An unsplit convolutional perfectly matched layer improved at grazing incidence for the seismic wave equation. *Geophysics*, 72(5):SM155–SM167.

Kurzmann, A. (2012). *Applications of 2D and 3D full wavform tomography in acoustic and viscoacoustic complex media.* PhD thesis, Karlsruhe Institute of Technology.

Kurzmann, A., Köhn, D., and Bohlen, T. (2008). Comparison of acoustic full waveform tomography in the time- and frequency-domain. In *Extended Abstracts, 70th EAGE Conference & Exhibition.*

Kurzmann, A., Köhn, D., Przebindowska, A., Nguyen, N., and Thohlen, T. (2009). 2D acoustic full waveform tomography: performance and optimization. In *Extended Abstracts, 71st EAGE Conference & Exhibition.*

Köhn, D. (2011). *Time Domain 2D Elastic Full Waveform Tomography.* PhD thesis, Christian-Albrechts-Universität zu Kiel.

Lay, T. and Wallace, T. C. (1995). *Modern global seismology*, volume 58 of *International Geophysics Series.* Academic Press.

Leveille, J. P., Jones, I. F., Zhou, Z.-Z., Wang, B., and Liu, F. (2011). Subsalt imaging for exploration, production, and development: A review. *Geophysics*, 76(5):WB3–WB20.

Lévêque, J.-J., Rivera, L., and Wittlinger, G. (1993). On the use of the checker-board test to assess the resolution of tomographic inversions. *Geophysical Journal International*, 115(1):313–318.

Liang, W.-g., Yang, C.-h., Zhao, Y.-s., Dusseault, M., and Liu, J. (2007). Experimental investigation of mechanical properties of bedded salt rock. *International Journal of Rock Mechanics and Mining Sciences*, 44(3):400–411.

Lin, Q. (2003). A study of long-offset seismic imaging with an upgraded physical modeling system. Master's thesis, University of Houston.

Martin, R. and Komatitsch, D. (2009). An unsplit convolutional perfectly matched layer technique improved at grazing incidence for the viscoelastic wave equation. *Geophysics*, 179(1):333–344.

Mora, P. (1987). Nonlinear two-dimensional elastic inversion of multioffset seismic data. *Geophysics*, 52(9):1211–1228.

Nocedal, J. and Wright, S. J. (1999). *Numerical Optimization.* Springer, New York.

Paffenholz, J. (2001). Sigsbee2 synthetic subsalt dataset: image quality as function of migration algorithm and velocity model. In *2001 SEG Annual Meeting.*

Pratt, G., Shin, C., and Hicks, G. (1998). Gauss–Newton and full Newton methods in frequency–space seismic waveform inversion. *Geophysical Journal International*, 133(2):341–362.

Ravaut, C., Alerini, M., Pannetier-Lescoffit, S., and Thomassen, E. (2008). Sub-salt imaging by full-waveform inversion: a parameter analysis. In *Extended Abstracts, 70th EAGE Conference & Exhibition.*

Reynolds, J. M. (1997). *An introduction to applied and environmental geophysics.* Wiley.

Ricker, N. (1953). The form and laws of propagation of seismic wavelets. *Geophysics*, 18(1):10–40.

Sirgue, L. (2006). The importance of low frequency and large offset in waveform inversion. In *Extended Abstracts, 68th EAGE Conference & Exhibition.*

Sirgue, L. and Pratt, R. G. (2004). Efficient waveform inversion and imaging: A strategy for selecting temporal frequencies. *Geophysics*, 69:231–248.

Tarantola, A. (1984). Inversion of seismic reflection data in the acoustic approximation. *Geophysics*, 49(8):1259–1266.

Tarantola, A. (1986). A strategy for nonlinear elastic inversion of seismic reflection data. *Geophysics*, 51(10):1893–1903.

Tarantola, A. (2005). *Inverse problem theory and methods for model parameter estimation.* SIAM, Philadelphia, Pa.

Vigh, D., Starr, E. W., and Elapavuluri, P. (2009). Acoustic waveform inversion vs. elastic data. In *2009 SEG Annual Meeting*.

Virieux, J. and Operto, S. (2009). An overview of full-waveform inversion in exploration geophysics. *Geophysics*, 74(6):WCC1–WCC26.

# List of Figures

# List of Tables

# Appendix

## A Computational resources

In order to obtain the FWI results I used high performance computers:

- *InstitutsCluster 2* (IC2) of the Steinbuch Centre for Computing (SCC) at the KIT,
- *HP XC3000* (HC3) of the SCC at the KIT,
- *Jülich Research on Petaflop Architectures* (JuRoPA) of the Jülich Supercomputing Centre.

The speed of the FWI calculation depends heavily on the used compiler. A comparison of Open Message Passing Interface (Open MPI) in combination with various compiler produced computing performances displayed in Table A.1:

Table A.1: Computing time of Open MPI in combination with various compiler.

| compiler | computational time in min per iteration | comment |
|---|---|---|
| gcc 4.1.2 | 3.50 | - |
| gcc 4.3.4 | 5.60 | - |
| intel 11.1.080 | 2.50 | - |
| intel 12.1.3 | 2.53 | incorrect reorganisation of domain decomposition |
| intel 12.1.11 | 5.88 | - |

The choice of the MPI implementation influences the computational time (Figure A.1). Various tests have shown that Intel MPI in combination with an Intel compiler is the best choice. The fastest and best results were produced by the combination of *impi 4.1.0* and the *Intel compiler 12.1.13*. For acoustic FWI one iteration was performed in about 20 s on 400 cores ($8000\,\frac{\mathrm{s}}{\mathrm{core}\cdot\mathrm{iter}}$). The elastic FWI DENISE was able to perform one iteration in about 200 s on 350 cores ($70000\,\frac{\mathrm{s}}{\mathrm{core}\cdot\mathrm{iter}}$). The greater computational time of the elastic code is caused by higher modelling efforts and a different parallelisation strategy.

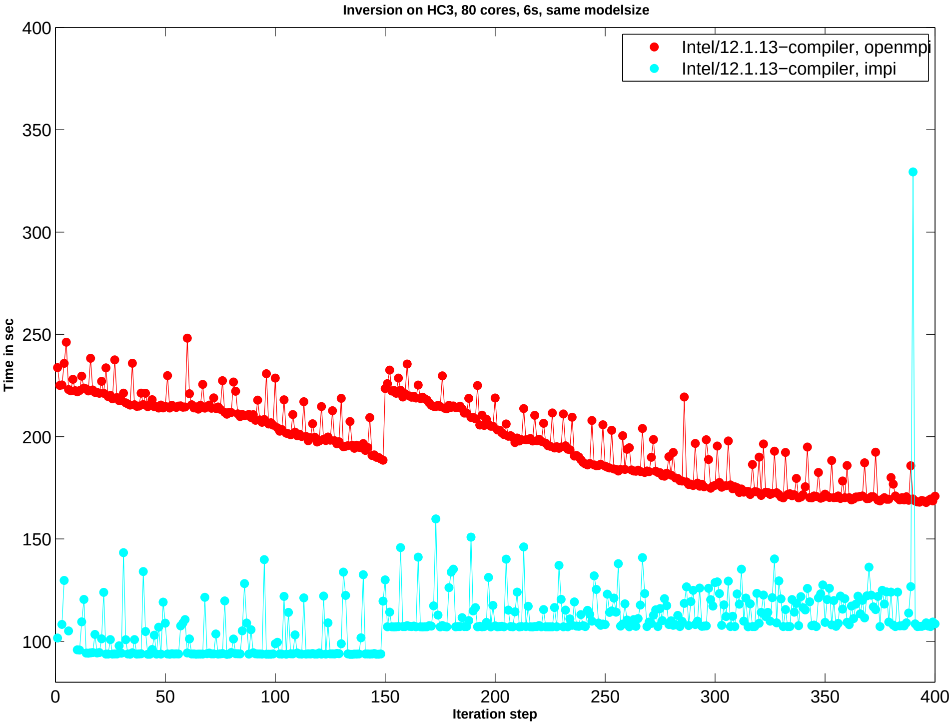

Figure A.1: Computational time per iteration for Open MPI and Intel MPI with the same Intel compiler, computed on HC3.

# B Danksagung/Acknowledgements

Zum Abschluss möchte ich noch all jenen danken, die mich bei der Erstellung der Arbeit unterstützt haben.

Thomas Bohlen danke ich für die Ermöglichung dieser Arbeit und für die wichtigen Tipps während der gesamten Arbeitszeit. Auch möchte ich mich bei Friedemann Wenzel für die Übernahme des Korreferates bedanken.

Fugro Seismic Imaging Ltd. danke ich für die Bereitstellung des Datensatzes und zugehöriger Informationen, mit denen ich die synthetischen Studien in dieser Arbeit möglichst realistisch aufbauen konnte. Ein großer Dank geht vor allem an Thomas Hertweck als Kontaktperson, das super Praktikum 2011 bei Fugro Seismic Ltd. in Swanley, das auch mein Interesse für das Subsalt Imaging geweckt hat, und die Anmerkungen zur schriftlichen Ausarbeitung.

André Kurzmann und vor allem Anna Przebindowska danke ich für die hervorragende Betreuung und die vielen Diskussionen und Anregungen während des gesamten letzten Jahres.

Der ganzen Arbeitsgruppe inklusiv Claudia Payne danke ich für die zahl- und aufschlussreichen Gespräche und Diskussionen. Ihr seid eine super Unterstützung und ich habe immer ein offenes Ohr für Fragen und Probleme gefunden.

Ein großer Dank geht natürlich auch an das Masteranden-Zimmer 104. Laura und Matthias, das Arbeiten mit euch hat echt Spaß gemacht, wie auch die Diskussionen über wissenschaftliche und alle anderen Themen.